

CALIFORNIA STATE UNIVERSITY, NORTHRIDGE

GEOPHYSICAL SITE CHARACTERIZATION USING
GEOMORPHOLOGY, GEOLOGY AND
INTEGRATED DIGITAL IMAGING METHODS ON
SATELLITE DATA

A thesis submitted in partial fulfillment of the requirements

For the degree of MASTER of Science in

Interdisciplinary Studies,

Geology and Geophysics

By

Alan Yong

June 2007

The thesis of Alan Yong is approved by:

Susan E. Hough, Ph.D.

Date

Helen M. Cox, Ph.D.

Date

Gerry W. Simila, Ph.D., Chair

Date

ACKNOWLEDGEMENTS

My gratitude goes to my peers, the staff and the faculty at Pasadena City College, at CalState Northridge and at the Caltech Seismological Lab.

I also extend my gratitude to my colleagues at the U.S. Geological Survey who have shaped and will continue to shape my professional development. They include Sue Hough, Rufus Catchings, Bob Dollar, Arnie Acosta, Linda Curtis, Sandra Dedeaux, Karen Felzer, Ned Field, Gary Fuis, Doug Given, Ken Hudnut, Katherine Kendrick, Nancy King, Lucy Jones, Erik Pounders, Michael Rymer, Stan Schwarz, Dave Wald, Allan Walter, Bruce Worden, and others that I may have inadvertently missed.

I am especially grateful to my advisors for their direct contributions to my intellectual and professional growth. Specifically, I am grateful to Gerry Simila (Professor of Geology) and Sue Hough (Seismologist/USGS Scientist-In-Charge), for providing the opportunities, the prospects and the guidance that made this benchmark a possibility and now, a reality. And to Helen Cox (Professor of Geography), for her insightfulness and most importantly, her ability to declare, at any point that “the emperor is not wearing any clothes”.

To my family, I am grateful for my mother’s unwavering love and compassion and my father’s pride and joy. To my brothers, for all we have gone through and will go through, together.

To my wife, Karolyn, I am grateful for everything, and more poignantly, for her love, vigilance, fortitude and her faith in us, and although inseparable, in me alone, while I took this short and meaningful journey. Karolyn has indicated many times that she vicariously lives our love for the sciences through my work. As in all things, I share this degree with her.

And lastly Zöe, for whom I am grateful because only she can provide what no human can possibly give.

Partial support for the project was provided by the U.S. Geological Survey and by the CSUN CATALYST program, funded by NSF-GEO (NSF-GEO-0119936 (2001-2005) and 0503609 (2005-2009)).

TABLE OF CONTENTS

SIGNATURE PAGE	ii
ACKNOWLEDGEMENTS	iii
ABSTRACT	vii
INTRODUCTION	1
Problem Definition	2
Approach and Method	3
Objectives and Significance	4
THEORETICAL BACKGROUND	5
Seismic Ground Motions	5
Attenuation Relations	6
Site Effects	7
Remote Sensing System and Analysis	9
Detection and Measurement of Spectra	9
Spectra and Object Interactions and Spectral Signatures	10
STUDY AREA	11
Physiography	11
Geology	12
Seismotectonics	12
DATA	14
APPROACH	16
METHODS	17
Relative DEM (Object-oriented) Analysis	19

Multi-resolution Analysis, Extraction and Segmentation	20
Workflow	21
Preprocessing of Imagery	21
Multi-resolution Segmentation	22
Class and Class Hierarchy Definition	25
Classification	25
Spectral (Pixel-based) Imaging/Analysis	26
Absolute Band Composite Method	28
Assignment of Shear-wave Velocity Ranges	31
SUMMARY AND CONCLUSIONS	32
REFERENCES	38
TABLES	46
FIGURES	48
APPENDIX A	63
Seismic Ground Motions	63
Propagation and Attenuation of Seismic Waves	63
Amplification of Seismic Waves	69
APPENDIX B	75
Remote Sensing Principles	75
The Remote Sensing System	76
The Spectral Source and Spectra	76
Transmission	77
Absorption	78

Reflectance	78
Scatter	79
APPENDIX C (rearrange section order)	81
ASTER Remote Sensing System	81

ABSTRACT

GEOPHYSICAL SITE CHARACTERIZATION USING GEOMORPHOLOGY, GEOLOGY AND INTEGRATED DIGITAL IMAGING METHODS ON SATELLITE DATA

By

Alan Yong

MASTER of Science in
Interdisciplinary Studies,
Geology and Geophysics

This project explores the use of remote-sensing imagery and integrated digital imaging analysis methods to improve the estimation of seismic hazards in the Islamabad, Pakistan region. The principal utility of the resultant map is to characterize the local landform features in terms of their potential to amplify ground motions generated by large-magnitude earthquakes. Because these landform features dramatically affect ground shaking during an earthquake, precise maps are critical for the development of urban hazard maps that identify areas of highest hazard within a greater metropolitan region. This project validates that remote-sensing imagery, along with an integrated

pixel-based and object-oriented digital imaging analysis methods, has significant potential to characterize the detailed geomorphology and geology. To demonstrate this potential, the project produces a first-order site conditions map of the Islamabad study area. Information about local geomorphology and geology from ASTER (Advanced Space-borne Thermal Emissions and Reflectance) satellite imagery are extracted through the use of the eCognition (object-oriented) multi-resolution segmentation software program on the ASTER relative DEM imagery and the use of the ENVI (pixel-based) software program on the ASTER spectral imagery. The resulting geomorphic units in the study area are classified as mountain, including the Margala Hills and the northeast trending linear ridges, piedmont, and basin terrain units. The local geologic units are classified as limestone, in the Margala Hills and the linear ridges, and sandstone rock-types for the piedmonts and basins, which correlate with the local geology. Then, the geomorphology and geology are correlated with the expected compositional rigidity for correlation with the average seismic shear-wave velocity through the upper 30 m of the subsurface (V_{s30}). In the resultant map image, the high relief and limestone regions of the Margala Hills are assigned the highest velocity range ($V_{s30} > 500$ m/s), the Islamabad and Rawalpindi regions (piedmont bench), just south of the Margala Hills, are assigned with the intermediate velocity range ($V_{s30} = 200-600$ m/s), and the basin, to the south, is assigned with the lowest velocity range ($V_{s30} < 300$ m/s). The resultant map is determined to be a first-order site conditions map and a preliminary map of potential site amplification in the study area.

INTRODUCTION

This project develops and applies automated digital imaging analysis methods by integrating pixel-based and object-oriented methods on ASTER (Advanced Space-borne Thermal Emissions and Reflectance) satellite imagery to characterize seismic site effects based on the interpretations of geomorphologic and geologic features. Although the methods employed in this project have already been applied in various disciplines (for example, Yan, 2003; Agarkov et al., 2005; Argialas and Tzotsos, 2006), to the knowledge of the author, only a limited approach has previously been attempted (for example, Romero and Rix, 2001; Wald and Allen, 2007) for application in seismic hazards analysis, such that the approach and scope applied in this project represent the first attempt of its kind.

Site characterizations are a critical part of seismic hazard assessments because local geology (Bard and Bouchon, 1980; Bard and Gabriel, 1986; Aki, 1988; Boore and Joyner, 1997) and topography (Bard and Tucker, 1985; Geli et al., 1988; Sánchez-Sesma and Campillo, 1993) have long been known to have a substantial affect on earthquake ground motions (for example, Wood, 1908; Reid, 1910; Faccioli, 1991; Kawase, 2003). For example, the 1989 M6.9 Loma Prieta earthquake, also known as the “World Series Quake,” occurred nearly 100 km away from the densely populated San Francisco Bay Area, yet it caused severe damage in parts of the Bay that are underlain by especially soft sediments. Later examples of local site effects include the collapse of part of Interstate-10 in Los Angeles following the 1994 M6.4 Northridge earthquake, and damage in the capital city of Islamabad, Pakistan, following a 2005 M7.6 Muzaffarabad earthquake. Damage in Los Angeles and Islamabad occurred at considerable distances away from the

respective epicenters of the earthquakes. In these and many other cases, damage could be attributed to the amplification of seismic waves in the shallow subsurface.

To better predict future earthquake ground motions throughout an urban region such as the metropolitan areas in southern California, it is necessary to improve detailed maps of local rock types, or geologic units (Wills et al., 2000; Wills and Clahan, 2006). For the greater Islamabad metropolitan area, it is necessary to develop detailed maps with similar thematic criteria (Yong et al., 2006b; Yong et al., 2006c; 2007). To relate the rock types to their expected amplification, one must estimate shear-wave velocity (a proxy for impedance) (Gueguen and Palciauskas, 1994) for each lithologic unit (Borcherdt, 1970; Park and Elrick, 1998). Classifications of site conditions are traditionally made based on V_s30 values, **the average seismic shear-wave velocity through the upper 30 m of the subsurface** (Fumal and Tinsley, 1985; Tinsley and Fumal, 1985; Anderson et al., 1996; Park and Elrick, 1998; Wills and Silva, 1998) and are added as a correction term to ground motion models or attenuation relations (for example, Abrahamson and Silva, 1997; Boore et al., 1997; Campbell, 1997; Sadigh et al., 1997) used to predict the response of site-specific ground motions during strong earthquakes (Borcherdt, 1985; Field and Petersen, 2000).

Problem Definition

Despite the recognized importance of site effects, efforts to develop site conditions maps have been hampered for decades by their reliance on conventional geological mapping techniques (Fumal and Tinsley, 1985; Petersen et al., 1997; Park and Elrick, 1998). Recent investigations (Wills et al., 2000; Wills and Clahan, 2006) continued to use conventional mapping techniques to characterize the local geology

throughout California. Most notably, Wills et al. (2000) presented a site conditions map based on rock-types ranging from hard rock to very soft sediments for the entire state. The Wills et al. (2000) map, however, is compiled at a small scale (1:250,000), which lacks the precision for reliable seismic zonation (Tinsley et al., 2004). Wills et al. (2000) investigated the precision of their map and showed that their map is expected to have an uncertainty rate of 24% when used to assign site characterizations of individual locations.

This project addresses the following problems: (1) Site factor is vital to ground motion analysis and characterization, but the most accurate site conditions map (Wills et al., 2000) for California has a high uncertainty rate; and (2), in other seismically active regions, such as key metropolitan areas in Pakistan, no comparable site condition maps are available.

Approach and Method

As a test case, without *a priori* information about local conditions, this project applies automated digital imaging analysis methods on satellite-produced, remote sensing imagery to meet the need for precise and uniform map information for the Islamabad, Pakistan region. Based on known correlations between geology and V_s30 (Wills et al., 2000; Wills and Clahan, 2006), and the image-based interpretations of terrain relief and composition of Islamabad, a first-order site conditions map is produced.

The imagery, ASTER radiometric data, is acquired through collaboration with Michael J. Abrams, ASTER Science Team Leader at NASA-JPL. Generalized terrain units affecting seismic site conditions are identified based on observations by Wills and Clahan (2006). An expert-knowledge base for automated object-oriented, multi-resolution segmentations and classifications of the ASTER imagery is constructed in the

eCognition/Definiens Professional 5.0, or eCognition (Definiens, 2006) commercial software, to extract and define the terrain units affecting site conditions. Next, automated pixel-based spectral analyses are performed in the ITT-VIS ENVI+IDL 4.3, or ENVI (Environment for Visualizing Images) (ITT-VIS, 2006), digital imaging analysis commercial software to verify the rigidity (hardness) of the terrain units through the interpretation of the terrain rock-type. Next, the rock-type is independently verified through literature review. Finally, using the Vs30-lithology correlations observed by Wills and Clahan (2006), the extracted terrain units from eCognition and the observed rock-types from ENVI, a first-order site conditions map is produced.

Objectives and Significance

This project's overall objective is to improve the predictions of future earthquake shaking intensities for metropolitan regions such as Islamabad. Islamabad is chosen as a test case to demonstrate the utility of the approach for regions where site effects are expected to be a significant component of seismic hazards, yet are not incorporated in current hazard maps. Regions in California and Islamabad share similar characteristics in their tectonic settings. These similarities are significant because they allow this project to directly apply the results of Wills et al. (2000), and Wills and Clahan (2006) geology and Vs30 correlations to the Islamabad regions.

To the knowledge of the author, this project produces the first ever site conditions map of the region surrounding Islamabad, Pakistan. The approach and methods developed in this project is currently applied to an on-going collaborative effort that includes the author, the U.S. Geological Survey (USGS), National Aeronautic and Space Administration Jet Propulsion Laboratory (NASA-JPL) and California Geological Survey

(CGS), to improve the Wills et al. (2000) California statewide site conditions map (Yong et al., 2006a).

THEORETICAL BACKGROUND

To provide a basis for the approach and methods used in this project, the following sections consist of focused background materials about seismic site effects and remote sensing system and analysis. These two subjects are from two separate, yet similar disciplines: seismology and remote sensing. Specifically, both disciplines use a similar form of detection method to describe natural phenomena. For example, in seismology, seismic energy, in the form of acoustic waves, are detected by sensors that measure the movements of an inertial mass set into motion by the earthquake; and, in remote sensing, electromagnetic (EM) energy, in the form of EM waves, is detected by optical scanners measuring the intensity of the incoming spectra. For more detailed information about seismology and remote sensing beyond what is presented below, refer to the additional sections in Appendix A and Appendix B, respectively.

Seismic Ground Motions

Knowledge of the structure and nature of the Earth's interior has been derived primarily from observations of seismic disturbances released by earthquakes. These disturbances are manifested as ground shaking during an earthquake. The amount of ground shaking from the associated seismic hazard is determined by the response of the ground to the seismic disturbance. In general, seismic ground motion intensity is affected by: (1) the seismic source, (2) propagation path, and (3) site effects. Effectively, site effect or site response is essentially a function of specific site conditions. Therefore, site

conditions, specifically, the effects of surface geology (ESG), are the properties that this project describes.

Both the seismic source and path effects will also greatly influence the behavior of the arriving seismic wave. Nevertheless, it has been observed (Anderson et al., 1996) that although the upper 30 m represents only 1% of the path from the source, the shallow subsurface has an enormous affect on ground motion intensity. Earlier (Borcherdt, 1970; Fumal, 1978; Faccioli, 1991) and subsequent (Boore and Joyner, 1997; Field and Petersen, 2000; Wills and Clahan, 2006) studies have also directly or indirectly taken accounted the strong influence of the upper 30 m layer on their ground motion calculations.

Attenuation Relations To predict ground motion amplitudes for a given magnitude and distance, mathematical models known as attenuation relations are used. One type of model, referred to as empirical attenuation relations, is derived from regression analysis of recorded ground motion parameters. Where sparse seismic records exist, theoretical attenuation relations based on numerical models and synthetic seismograms have been developed. In general, all attenuation relations provide a regional scale formulation of ground motion as a function of distance from the seismic source.

Because the attenuation relations are region dependent, the type of tectonic environment has an enormous impact on the predictive model. Campbell (2003) suggested four types of tectonic environments: (1) shallow crustal earthquakes in active tectonic environments; (2) shallow crustal earthquakes in stable tectonic environments; (3) intermediate depth or intraslab earthquakes (Wadati-Benioff earthquakes); and (4) earthquakes along the interface of two subducting plates. Using an appropriate

attenuation relation derived from local data or from recordings in a tectonically similar region, ground motion can be predicted for any future earthquake.

Site Effects For a site-specific estimation of ground motion, a site effects term is incorporated into either type (empirical or theoretical) of attenuation relation to account for the ground response due to local site conditions. One approach for characterizing site effects is to acquire *in situ* measurements based on methods that record induced seismic energy at the sites of interest (for example, Kawase, 2003). Another approach is to correlate the effects of surface geology (local site conditions) with ground motions and apply the observed velocities to other sites with similar site conditions (Borcherdt, 1970; Fumal and Tinsley, 1985; Boore and Joyner, 1997; Wills et al., 2000; Wills and Clahan, 2006).

As a rule, the type of approach that is appropriate for an investigation depends on the intended application of the results. The *in situ* measurement method is by far more precise than the geologic-correlation method, but it is prohibitively expensive and impractical when numerous site measurements are needed. On the other hand, measured velocities have been observed to vary tremendously in a short distance from the locations of measurement (Wills and Silva, 1998).

Early on, Borcherdt (1970) observed “marked amplitude variations which are related consistently to the geologic setting of the recording site.” Fumal (1978) was able to identify and define several physical parameters that are seismically distinct for geologic map units. Later, for the purpose of seismic zonation, Fumal and Tinsley (1985) mapped the greater Los Angeles area based on the seismically distinct geologic map units previously defined by Fumal (1978). Boore and Joyner (1997) defined a generic site as

“one whose velocity at shallow depths equals the average of those from the rock sites sampled by the borehole data,” and assigned generic soil sites and rock sites to be those with V_{s30} values of 310 m/s and 620 m/s, respectively. Using the Boore and Joyner (1997) generic rock site relationship, Petersen et al. (1997), and Park and Elrick (1998) were able to extend and refine the work of Fumal and Tinsley (1985).

Most recently, a California statewide preliminary site conditions map by Wills et al. (2000) provided the most comprehensive map compilation based on previous works (Fumal and Tinsley, 1985; Petersen et al., 1997; Park and Elrick, 1998) and available measurements (556 profiles) of shear-wave velocity data. Wills and Clahan (2006) expanded the eight NEHRP-based site categories (Table 1) from the Wills et al. (2000) map to 19 geologic-based categories (Table 2) to accommodate the need for a more precise consideration of site conditions. The need for higher precision is in part driven by the recent efforts to replace older empirical ground motion models (for example, Abrahamson and Silva, 1997; Boore et al., 1997; Campbell, 1997; Sadigh, 1997) with new relations developed by the Next Generation Attenuation (NGA) project (http://peer.berkeley.edu/products/nga_project.html). The expanded categories were based on the subdivision of geomorphic units and their geologic properties such as grain sizes (Wills and Clahan, 2006). In addition, the Wills and Clahan (2006) also took into account: (1) newly available shear-wave velocity measurements; (2) known thicknesses (depth) of the geologic units; (3) the variability of terrain slope; and (4) the nature of the surface roughness. The additional geologic conditions were proposed and/or observed earlier by other studies (Fumal, 1978; Fumal and Tinsley, 1985; Tinsley and Fumal, 1985), but were not included for consideration in the compilation of the Wills et al.

(2000) preliminary map. It is noteworthy that Wills and Clahan (2006) did not provide a statewide map because the geologic information for most of the region was still incomplete or not readily available.

Remote Sensing System and Analysis

Remote sensing is defined as the unobtrusive detection of information about the existence of an object without being in direct physical contact with the object of interest. The detected information is usually about the changes that the object imposes on its surrounding environment. Based on *a priori* knowledge about how the state of the surrounding environment is influenced by the type of change imposed, the object is identified.

Today, remote sensing systems are flown on aircraft in low altitude or on satellite platforms launched into orbit by spacecraft. Commonly, each system is specially designed to acquire data for specific purposes, such as ASTER for geologic investigations. Regardless of its purpose, a remote sensing system fundamentally consists of (1) a source of energy, (2a) an object that interacts with the energy or (2b) an object that is itself a source of energy, (3) a resultant radiance from the object, and (4) a sensor that detects the radiance captured by a collector and measures the properties of the radiance (Elachi and van Zyl, 2006). In this project, the source is solar energy that is reflected back from the Earth's surface and detected as EM radiation.

Detection and Measurement of Spectra The radiation emitted, reflected or scattered from an object generates a radiant flux density (emittance or rate at which energy passes a unit area). The response of the environment to the emittance contains important information about the object's properties (Elachi and van Zyl, 2006). To measure the

state of the surrounding environment influenced by the object's reaction to the EM radiation, a collector and detector setup is used in a remote sensing system.

For measurements and recordings of spectra in the visible (VIS) to thermal infrared (TIR) range (0.4-14 μm), the collector component, or collecting aperture, consisting of a lens or reflecting surface focuses the intercepted energy onto the detector (Elachi and van Zyl, 2006). Then, detection follows by the transformation of EM energy into another form of energy, such as heat, electric current, or state change. In the case of spectrometers and radiometers, total radiant energy flux at a specific location is measured as a function of wavelength (Elachi and van Zyl, 2006).

Spectra and Object Interactions and Spectral Signatures The interaction of the EM waves with an object is strongly dependent on the frequency of the wave (Elachi and van Zyl, 2006). As the wave interacts with the material, the electrons, molecules, and/or nuclei respond and there is an exchange of energy between the wave and the material. The reactions of the atomic particles include rotation, vibration and displacement, which affect the amount of radiation absorbed by the object. In the VIS-NIR regions (0.4-1.3 μm), vibrational and electronic energy transitions play the key role in the identification of rocks and their constituent minerals (Elachi and van Zyl, 2006). These energy transitions produce interactions in broad spectral bandwidths that include molecular vibration, ionic vibration, crystal field effects, charge transfer, and electronic conduction. Some of the spectral features in this wavelength region include (Elachi and van Zyl, 2006): (1) a steep fall-off of reflectance in the VIS spectrum toward the ultra-violet (UV) and an absorption band between 0.84 and 0.92 μm (NIR) that is associated with the Fe^{3+} electronic transition, characteristic of iron oxides and hydrous iron oxides (collectively known as

limonite or iron ore); (2) a sharp increase mesophyll scattering near 0.75 μm , which is commonly used in mapping vegetation; (3) the specific positions of the restrahlen bands (regions of metallic-like reflection) near the mid-IR (MIR) region (8-14 μm) associated with the Si-O fundamental stretching vibration, which are diagnostic of the major types of silicates (Fig. 1). In the TIR region (3-14 μm), the emitted radiation depends on the emissivity of the Earth's surface and local temperature and the radiation received will include the effects of the overlying atmosphere (Elachi and van Zyl, 2006).

STUDY AREA

The study area or area of interest (AOI) is the region that surrounds Islamabad, the capital of Pakistan. It is located just north of the old city of Rawalpindi and has a population of 1.3 million (Williams, 1999). The AOI is also the 60 \times 60 km swath that coincides with the spatial extent of the AST14DEM footprint (Fig. 2), which is slightly smaller than the corresponding AST_L1B footprint (see Appendix C). Because of the angle of inclination of the satellite, the ASTER coordinate values for the northwest (33.97, 72.66), northeast (33.87, 73.33), southeast (33.32, 73.18) and southwest (33.42, 72.51) corners do not align as right angles (Fig. 2).

Physiography

The terrain of the AOI consists of plains and mountains with a general physiography that trends east-northeast (Williams, 1999). As a part of the lower and outer Himalayas (Williams, 1999), the northeastern part of the AOI lies in the mountainous terrain referred to as the Margala Hills, which consists of a series of ridges with altitudes of approximately 1,600 m near Islamabad. South of the Margala Hills is a southward sloping piedmont bench (Williams, 1999) where the Islamabad and

Rawalpindi urban developments are situated. Further south, the Soan River valley extends outward to the plains of the Potwar Plateau beyond the AOI.

Geology

Williams (1999) divided the structure and lithology of the Islamabad and Rawalpindi area into three zones: (1) the northern mountainous Margala Hills that consist of folded and thrust-up limestones and shales (Zulfiqar et al., 2005; Munir and Butt, 2007); (2) south of the Margala Hills, a southward-sloping piedmont bench that consists of truncated and folded sandstones and shales, in addition to buried and exposed ridges of sandstones and shales by alluvial cover west of Rawalpindi; and (3) the asymmetric syncline of the Soan River valley that consists of beds of fluvial sandstone, mudstone and conglomerate. As a depositional system, the piedmont accumulates silt and alluvial gravel from the Margala Hills, which eventually spreads and fills the wide plains of low relief (Williams, 1999). Due to the dry climate, well developed soils are scarce in the Islamabad area (Williams, 1999).

Seismotectonics

The AOI is part of a region wide regime of compressional tectonics that continually folds and thrusts the local geology. The Margala Hills are an intensely deformed tectonic belt that represents the uplift of the Peshawar basin that is part of the active Himalayan foreland where fold and thrust belts form the collision zone between the Indian and Eurasian plates (Zulfiqar et al., 2005).

Zulfiqar et al. (2005) speculated that the main seismogenic features that affect seismic hazards in the Islamabad and Rawalpindi area are primarily active thrust faults in proximity to the cities. These include:

- Main Boundary Thrust (MBT)
- Margala Fault
- Hazara Thrust
- Panjal Thrust
- Jhelum Fault
- Manshera Thrust
- Murree Thrust

The closest fault systems are: (1) the MBT, which is approximately 270 km long and extends along the Himalayan Front, passing about 1 km from the Margala Hills; (2) the Panjal-Khairabad fault, which passes north of the Margala Hills at approximately 26 km; and (3) the Hazara thrust fault system, which has three branches in the Margala Hills with the nearest trace approximately 15 km from Islamabad (Zulfiqar et al., 2005). As a side note about the seismogenic and geologic history of this region, the Hazara fault zone was developed when the limestone of Margala Hills was thrust up and when the sandstone and shale was folded in the piedmont bench to the south (Williams, 1999).

Also noteworthy is the most recent large earthquake (M7.6) that occurred on October 8, 2005 near Muzaffarabad in the Kashmir region, approximately 100 km northeast of Islamabad, which caused about 86,000 in fatalities, 100,000 in injuries and numerous structure collapses, including buildings in Islamabad and Rawalpindi (NEIC, 2005). Based on initial accounts, the USGS (NEIC, 2005) reported that the Islamabad and Rawalpindi area experienced an overall Modified Mercalli Intensity (MMI) level of VI. This intensity level corresponds to shaking that is: “Felt by all, many frightened. Some heavy furniture moved; a few instances of fallen plaster — Damage slight”. Although damage was light, several buildings did collapse in these two cities. The USGS also reported (NEIC, 2005) that the maximum MMI level experienced in the Islamabad region was level VIII: “Damage slight in specially designed structures; considerable

damage in ordinary substantial buildings with partial collapse — Damage great in poorly built structures — Fall of chimneys, factory stacks, columns, monuments, walls — Heavy furniture overturned”.

DATA

Two sets of ASTER imagery of the Islamabad region were recorded on November 3, 2005 and were acquired through the EOSDIS EDG via a collaborative agreement with ASTER Team Science Leader Michael Abrams of NASA-JPL. The first set of imagery consists of 14 discrete bands (AST_L1B) of spectra ranging from the VNIR-TIR (0.52-11.65 μm) region and the second set of imagery consists of the relative DEM Level-3 product (AST14DEM). For more detailed information about ASTER, refer to Appendix C.

The AST_L1B image is essentially a re-sampled image product with correction coefficients applied to the Level-1A raw data (Yamaguchi et al., 1998; Abrams et al., 2002). In AST_L1A data, geometric correction and radiometric calibration coefficients are appended but not applied; so, critical factors, such as parallax caused by the offset in detector alignment in the along-track direction and the inter- and intra-telescope registrations, are not accounted for (Abrams et al., 2002). The AST_L1B data apply these geometric and radiometric corrections. Atmospheric corrections are applied to Level-2 products, but not to Level-1, so the AST_L1B imagery used in this project are potentially contaminated by the effects of aerosols. Although this project primarily applies absolute band composite methods (Kahle et al., 1980; Kahle and Rowan, 1980) to discriminate surface lithology, the removal of atmospheric effects is not necessary because the climate is generally arid and dry.

The AST14DEM image is a Level-3 image product generated using Band 3 (0.78-0.86 μm) from the nadir-viewing (3N) and backward-viewing (3B) sensors, with an input spatial resolution of 15 m and an output spatial resolution of 30 m (Abrams et al., 2002). The digital elevation model (DEM) is based on an automated stereoscopic correlation method — a standard procedure for generating DEMs from digital stereo images (Hirano et al., 2003). The stereo-pair has a base-to-height ratio of 0.6 and an intersection angle of approximately 27.7° , which is close to ideal for a variety of terrain conditions (Fig. 3) (Hirano et al., 2003). As opposed to other modes (for example, cross-track) of data acquisition, the along-track mode (Fig. 3) of the ASTER system produces an approximately one-minute lag time between the acquisition of the nadir and backward images such that images forming the stereo-pairs acquire spectra in very similar environmental conditions, resulting in very consistent image quality (Hirano et al., 2003).

All spectral bands are recorded on November 3, 2005 and packaged on November 6, 2006 into a single file (.hdf) and accompanied by a metadata file (.hdf.met). For this analysis, the following data files were utilized:

AST_L1B_00311032005055851_20061106153759_31600.hdf,
AST_L1B_00311032005055851_20061106153759_31600.hdf.met,
AST14DEM_00311032005055851_20061106151557_26862.tif, and
AST14DEM_00311032005055851_20061106151557_26862.tif.met

The scene dimensions for the AST_L1B data vary with spatial and spectral resolutions. The 15 m resolution VNIR (Bands 1, 2, 3N and 3B) bands have pixel dimensions of 4980×4200 , the 30 m resolution SWIR (Bands 4, 5, 6, 7, 8, and 9) bands have pixel dimensions of 2490×2100 , and the 90 m resolution TIR (Bands 10, 11, 12,

13, and 14) bands have pixel dimensions of 830×700 . The data type is floating point. The scene dimensions for the AST14DEM are 2544×2436 , the data type is integer, and the storage format is the Tagged Image File Format. When comparing the AST_L1B and AST14DEM data, there is a noticeable difference in the spatial extent of the AST_L1B and AST14DEM footprints such that the footprint of AST14DEM is smaller than that of the AST_L1B. This is an effect caused by the use of moving windows to calculate the stereocorrelation between the 3N and 3B images (Abrams, 2007). The geographic projection for the data is Universal Transverse Mercator (UTM), Zone 43 North, and the datum is based on the World Geodetic System (WGS84).

The imagery were manually determined to be cloud free. Filtering for noise reduction was not necessary because no significant data corruption was apparent in the files used in this project.

APPROACH

The approach of this project employs the following methods (in order) on the ASTER imagery: (1) digital imaging analysis of the DEM for breaks in the spatial changes in elevation values (slope) and assignments of terrain units as classes (mountains, piedmonts and basins) (Yong et al., 2006c); (2) digital imaging analysis and discrimination of rock types (lithology) using spectral features (Kahle and Rowan, 1980; Abrams and Hook, 1995; Yong et al., 2007) in the ASTER bandwidths (VNIR-TIR); (3) comparison of the spatial distribution of the lithology and its spatial correlation with the pre-assigned terrain units to verify the composition of the terrain unit; (4) assignments of ranges of shear-wave velocity based on Wills and Clahan (2006) and the inferred rigidity of the terrain from the combination of terrain classes and spectral-based lithologic

discriminations of the terrain units and the associated lithology; and then, (5) verification of the identified lithology with independent investigations or observations in the AOI (Islamabad region).

METHODS

Digital imaging analysis methods are used for extracting information from the pixels within an image. Based on the value and distribution of the pixels, these methods primarily apply common techniques, such as geostatistics, to analyze the pixels in the image. On the other hand, it is in their application of these mathematical functions that these geostatistical methods differ. Two different applications, object-oriented and pixel-based digital imaging analysis approaches, are used in the project because each application has a specific capability to effectively perform a particular type of analysis and data processing task.

Fundamentally, each method is concerned with the pre-assigned value of the pixel and the position of the pixel in relation to others in the AOI. These pixels are usually assigned values in the form of digital numbers (DNs) representative of the raw data (for example, radiance) collected from a remote sensing system (Abrams et al., 2002). It is possible to work on imagery with pixels that are based on radiance values, but for this project, only pixels (AST_L1B and AST14DEM) based on DN are considered. The differences in the values of the DN for each individual pixel are used to explore the various unique features (for example, absorption bands) of spectra to extract information about the properties of the object. Depending on the spatial resolution of the image, there are instances where an object is the size of a single image pixel; in most instances, an object comprises multiple contiguous pixels positioned collectively in feature space.

To analyze groups of image pixels and the distribution of the collective groups of pixels for classification purposes, this project applies the object-oriented paradigm on the high spatial resolution ASTER DEM imagery. In this method, instead of applying geostatistics to each pixel for the analysis of their individual DN values and their spatial distribution, multiple pixels are analyzed in a construct referred to as image object space (Definiens, 2006). In image object space, object primitives (Definiens, 2006) are used for image classifications, rather than individual pixels. As an example, eCognition/Definiens Professional 5.0, or eCognition (Definiens, 2006), is an object-oriented, digital imaging analysis application program that takes into account predefined semantic and contextual information, among other information, to extract and classify pixels.

To analyze and visualize the value of the individual image pixels for the extraction of information about the properties of objects in an AOI, this project applies the pixel-based paradigm on the multi-spectral resolution ASTER imagery. In this method, geostatistics is applied to each pixel for the analysis of their individual DN to aid the interpretation of EM properties through multi-spectral analysis methods. Furthermore, visualization capabilities can be enhanced for image pixels that have low contrast but rich information through mathematical (statistics) transformation. Other pixel-based transformations include the preprocessing of data for geometric-related corrections, rectification of corrupted data and data format conversions. As an example, ITT-VIS ENVI+IDL 4.3, or ENVI (Environment for Visualizing Images) (ITT-VIS, 2006), is a pixel-based digital imaging analysis application program that uses geostatistics to analyze the spectra in image composites.

Relative DEM (Object-oriented) Analysis

To automatically identify the landforms that affect site conditions, one must first translate the features into terrain units. Terrain features can be described and categorized into simple topographic relief elements or units by parameterizing DEMs (Bolongaro-Crevenna et al., 2005). Using geomorphometric parameters (slope, aspect, azimuth, concavity/convexity, etc.) to class elemental terrain features into units (mountains, piedmonts, and basins) makes it possible to reapply the same parameters to other regions where similar geomorphology exists. For example, using only relative slope gradients as a geomorphometric parameter, Yong et al. (2006c) demonstrated that the same parameters used for Pakistan are applicable for a first-approximation of geomorphology in other regions that have distinctively different depositional environments, such as Turkey and Mozambique (Fig. 4). Also, geomorphometry offers a variety of additional approaches for defining terrain units, such as the classification of terrain feature parameters, filtering techniques, cluster analysis, and multivariate statistics (Pike, 2002; Bolongaro-Crevenna et al., 2005).

In this project, a ‘partial’ geomorphometric parameter, slope factor, is considered since the goal is a first-order approach to characterize terrain features for describing seismic site conditions. Technically, a complete set of geomorphometric parameters would include other factors, such as aspect, azimuth, and concavity/convexity. Practically, for local geologic site characterization, the terrain’s topographic relief is an adequate parameter to infer compositional rigidity of the site. But to verify compositional rigidity, site geology must be considered. This can only be performed through the spectral identification of lithology through the pixel-based spectral analysis

method described in the Spectral (Pixel-based) Imaging/Analysis section later. Currently, eCognition does not possess the same capabilities of ENVI to analyze and identify spectral features (absorption bands) in imagery.

Despite this limitation of eCognition, its object-oriented approach to segmenting pixels is very effective for classifying groups of contiguous pixels. This is because, for high spatial resolution data like the ASTER imagery, meso-scale terrain units are invariably represented by multiple contiguous pixels that are clustered collectively in a shape of some spatial extent. To effectively classify objects represented by multiple pixels in the image space or domain, shape, texture, color, context, and other morphological characteristics must first be considered. This is because, in the image space, image objects are the basic elements or primitives that fill the scene (Definiens, 2006; Navulur, 2006). For example, in the context of human recognition, when analyzing a scene, the elements of the scene are first broken down into various objects, based on the properties of the object (Theodoridis and Koutroumbas, 2006). Then, based on the person's experience, the objects are individually identified by the properties of the object and the object's contextual relationship to other elements in the scene. So, in both the physical space and the image space, the associated properties of the physical and image object primitives are distinguishable on the basis of properties such as shape, texture, color and contextual relationship. These parameters are also the same attributes outlined by Ray (1960) as recognition elements for the classic (manual) photo-geologic interpretation approach used in mapping terrain features.

Multi-resolution Analysis, Extraction and Segmentation Specifically, the project's object-oriented digital imaging analysis uses the eCognition algorithms for extracting

image objects. Once the image objects in the image space are analyzed, parameterized, extracted and segmented, they are then referred to as object primitives (Fig. 6A). Before any imaging work can be performed, a workflow is developed.

Workflow Development In this project, the workflow consists of: (1) a project (an eCognition abstraction) for managing and manipulating the data, the parameters, the functions, the intermediate results (object primitive levels) and the final results (classified map); (2) the definition of a segmentation strategy; (3) the definition of a class (based on parameters defined by user) hierarchy; (4) the assessment of parameters for the separation of classes based on the parameters; and (5) the classification of final object primitive level (Definiens, 2006).

Preprocessing of Imagery Prior to creating the project in eCognition, ENVI is used to deconvolve the AST_L1B data (in HDF format) to its 14 individual bands as 15 separate layers; Bands 3N and 3B are counted as one band because they both collect spectra in the same range, 0.78-0.86 μm , but have different viewing angles and so are deconvolved into separate layers. Then, the layer stacking of Bands (layers) 1, 2, and 3N are performed and the stack is converted to the TIFF format for the generation of a VNIR composite scene. In the eCognition display or any standardized application display (referred to as output space), Layer 1 (0.52-0.60 μm), Layer 2 (0.63-0.69 μm), and Layer 3N (0.78-0.86 μm) can be arbitrarily assigned to the RGB display channels: Red (R), Green (G) and Blue (B). When displaying ASTER VNIR composites, vegetation will not directly reflect the color green; thus, the composite is referred to as a false color image (Fig. 5). Instead, vegetation appears bright red when Layer 3N is assigned to the R display channel and will appear blue when Layer 1 is assigned to the same channel. This is because ASTER

does not collect spectra in the 'blue' region (0.4-0.49 μm) of the EM spectrum, which explains why the reflectance of color, such as green from vegetation observed in the VIS (0.4-0.7 μm) range, do not match colors observed in the NIR (0.52-0.86 μm) range (Abrams, 2007). In ASTER VNIR composites, the red vegetation is a direct result of the assignment of Band 3N to the R display channel where the chlorophyll and mesophyll in vegetation has the highest reflectance (~55%) in the NIR (0.78-0.86 μm) range, allowing the infrared (IR) reflectance to dominate the scene (Elachi and van Zyl, 2006; Abrams, 2007). As a result of Band 1 assignment to the R display channel and Band 3N to B, the blue color resulting from vegetation is caused by low reflectance (max ~15%) of chlorophyll in the mid VIS Band 1 spectral (0.52-0.60 μm) range (Elachi and van Zyl, 2006; Abrams, 2007). The creation of the VNIR composite is intended for use as a visual guide to assist in the parameterization phases during the iterations of segmentation and classification work that follow.

Next, the AST14DEM image is preprocessed during the project creation phase to exclude pixels in the image that are not related to the scene, such as the black color pixels of the image frame. As described in the DATA section, the minimum and maximum DN values in the array are -9999 and 1687, respectively. Pixels with -9999 values in the AST14DEM file represent no data and are masked out prior to any segmentation and classification work.

Multi-resolution Segmentation There are three types of segmentation algorithms defined in eCognition: the (1) multi-resolution segmentation algorithm; the (2) quadtree algorithm; and the (3) chessboard algorithm (Definiens, 2006). While the quadtree and chessboard algorithms performed faster, the multi-resolution segmentation algorithm was

chosen for the project because of its robustness and flexibility. Specifically, it takes into account important contextual information such as: the allowable degree of heterogeneity; the importance of color; the importance of shape; the importance of compactness; and the importance of smoothness (Definiens, 2006). Based on these parameters, hierarchical levels of object primitives are created (Fig. 6A) (Definiens, 2006). Through the pair-wise clustering of pixels (Fig. 6B), followed by a bottom-up region-merging technique, the segmentation process takes advantage of the resultant hierarchical network of object primitives that is cognizant of its neighbor-objects (Fig. 6C), its sub-objects (Fig. 6C), and its super-objects (Fig. 6C), creating contextual information (based on parent-child relations) on multiple scales (Definiens, 2006).

To extract mountain, piedmont, and basin units from the AST14DEM image of Islamabad, four object primitive levels of segmentations were found to be necessary. To define the four effective sets of contextual parameters that produced the fourth and final object primitive level, multiple iterations of manual selection and deletion, prior to establishing the parameters, were required. Only the VNIR composite was used as a guide. No other information about the character of the local terrain was used.

Based on the pair-wise clustering of pixels in the bottom-up region merging technique, the contextual parameters defined for this object primitive level was as follows: (1) a scale parameter of 10; (2) a shape parameter of 0.1; (3) a color parameter of 0.9; (4) a compactness parameter of 0.5; and (5) a smoothness parameter of 0.5. The first object primitive level (Fig. 7) produced a very dense scene filled with small object primitives that outlined the steep relief terrains (dark areas) in the northwest corner, the upper northeast quadrant, and the southwest quadrant.

The second object primitive level (Fig. 8) was derived from the first (previous) object primitive level with the following modified parameters: (1) a scale parameter of 50; (2) a shape parameter of 0.5; (3) a color parameter of 0.5; (4) a compactness parameter of 0.5; and (5) a smoothness parameter of 0.5. The second object primitive level scene maintains the outline of the steep terrains as characterized by the dark features in the first object primitive level. Other steep terrains, previously not apparent, start to take shape (Fig. 8).

The third object primitive level (Fig. 9) was based on the second (previous) object primitive level and the following modified parameters: (1) a scale parameter of 100; (2) a shape parameter of 0.7; (3) a color parameter of 0.3; (4) a compactness parameter of 0.5; and (5) a smoothness parameter of 0.5. This level reveals a more coherent segmentation result, in terms of distinguishable terrain features. The steep relief terrains (dark areas) in the northwest corner, the upper northeast quadrant, and the southwest quadrant implied in the first object primitive level have now taken form (Fig. 9). A ridge, not previously apparent at the top of the southwest quadrant has now also taken form.

In the fourth and final object primitive level, (Fig. 10) the object primitives were based on the third (previous) object primitive level and the following modified parameters: (1) a scale parameter of 250; (2) a shape parameter of 0.3; (3) a color parameter of 0.7; (4) a compactness parameter of 0.5; and (5) a smoothness parameter of 0.5. Here, based on visual comparisons with the VNIR composite, the mountain, piedmont and basin units, represented by the final object primitives, have now taken acceptable form (Fig. 10).

Class and Class Hierarchy Definition Next, the decision about defining a class and class hierarchy is made. A class is an eCognition construct used to describe, identify and group a collection of object primitives based on similarities in their characteristics. A class hierarchy is an eCognition construct that supports rule-based classifiers that invoke crisp threshold or fuzzy membership functions that are used to weigh the likelihood of an object primitive's membership to the available classes (Definiens, 2006).

The development of classes was necessitated by the need to differentiate the terrain units for seismic site characterization. On the other hand, based on the scope of this project, a class hierarchy was deemed unnecessary, since the terrain units or classes (mountains, piedmonts, and basins) do not necessarily follow a hierarchy. In addition, the spatial relationship of the units do not need to conform to adjacency rules (Yong et al., 2006c). For example, the adjacency of each terrain unit does not necessarily follow formulae such that a mountain feature (steep slopes) is adjacent to a piedmont (gentle intermediary slopes) and then a basin (relatively flat slopes) because a steep or vertical mountain front can be directly adjacent to a topographically flat basin floor (Rymer, 1987). For future considerations, a finer classification of terrain units, such as the sub-units (distal alluvial fan, mid-alluvial fan, and proximal alluvial fan) of a piedmont, based on class hierarchy will be identified.

Classification The classification of the object primitives in the final object primitive level is based solely on the Nearest Neighbor (NN) classifier in eCognition. Through the use of the nearest neighbor statistics method (Clark and Evans, 1954), the NN classifier fills a class predefined by the user through a supervised training approach that samples the representative values (integers) of the class. Then, based on the sampled

representative values and a distance metrics (neighborhood), the pixels or, in this case, object primitives are assigned to the associated class.

In this project, the NN classifier categorizes object primitives into classes based on sample object primitives, defined by the author. First, the samples are acquired through several iterations of manually selecting the optimal object primitives in the fourth and final object primitive level (Fig. 10). The optimal object primitives are defined as the best DN representation of the terrain units based on the correlation of the mean relative elevation values for each terrain unit to the visually interpretable terrain features in the VNIR composite. Second, based on the selected samples and the average distance between the centers of the object primitives, the NN classifier assigned the remaining object primitives into the classes defined by the author.

As an intermediate product, the terrain units can be assigned shear-wave velocity ranges, assuming that the units have typical velocities for mountains (hard rock), piedmonts (intermediate hard to soft rock) and basins (soft rock). But, to ascertain the hardness (rigidity) of these units for shear-wave velocity assignment, additional information, such as the composition of the units is required.

Spectral (Pixel-based) Imaging/Analysis

After the automated analysis, segmentation and classification of the terrain units through eCognition's algorithms, the next step is to verify that the compositions of the terrain units in the classification are as expected for mountain (hard rock), piedmont (moderately soft), and basin (soft) units. The verification of the expected hardness (rigidity) of the composition for the units is based on identification of the rock-type. This is done using spectral signatures.

There are two principal methods used for identifying a rock from its spectra. Each method can be refined for specific purposes, but their principles remain the same. One method is to identify a material by its absolute response to EM radiation. This method is a simple concept but yet very difficult to carry out because the radiation received at the sensor becomes contaminated by other signals while in transit to the remote sensing detector. To account for these path effects, complex and specific models are required to extract the object's spectrum from the received signal (Ninomiya et al., 2005; Rowan et al., 2005). The application of this method is only possible for instances when *a priori* information about the local conditions, such as atmospheric effects is available. In some conditions, where the climate is arid and dry and the atmospheric conditions are clear, near absolute response from only the object of interest is possible. The second method, known as band contrast or relative band depth ratio (RBD) (Crowley et al., 1989), is used to determine the presence of a material through the contrast of its spectral features to those of known objects. Based on the ratio of the contrast in certain spectral regions where the absorption features occur, the object can be identified.

In this project, a variation of the absolute response method, referred to as the Kahle and Rowan (1980) absolute band composite method, is used to analyze, identify and match spectra to known spectra-to-rock relationships. As mentioned in the data section, atmospheric contamination is not a concern because the ASTER imagery used is clear of the unfavorable factors that affect the signal received by the sensor. The arid and dry nature of the overall climate in the region also made the absolute band composite method applicable.

Absolute Band Composite Method The work of Kahle and Rowan (1980) verified that spectra acquired in laboratory conditions are comparable to spectra sampled in the field and acquired remotely (aircraft), and that these spectra can be employed to map lithologic features. After determining that the spectra from each acquisition vantage point matched laboratory spectra with high certainty, Kahle and Rowan (1980) mapped their field area based only on the remotely sensed data. Kahle and Rowan (1980) were able to duplicate the available lithologic map in their AOI and in some places, to identify other rocks that were previously not described.

Using ENVI, the AST_L1B (HDF) file is loaded and the bands are deconvolved into 15 separate layers of imagery. A composite image, comprising the ASTER TIR Bands 13 (10.25-10.95 μm), 12 (8.925-9.275 μm), and 10 (8.125-8.475 μm), assigned to display R, G and B, is created (Fig. 12). Emissivity and temperature control the intensity of brightness in TIR composite images. Because materials have distinctive emissivity characteristics, these composite images can be used to identify the specific material (Elachi and van Zyl, 2006). A material's temperature is greatly affected by local variations in the material's surrounding environment, so the material cannot be uniquely identified by its temperature alone. In addition, in TIR images: (1) emissivity does not vary a lot across a scene but does vary with wavelength; and, (2) temperature does vary across a scene but does not vary with wavelength (Adams and Gillespie, 2005), making these two characteristics useful in material identification. Using the ASTER TIR composite as an example, the distribution of the high intensity of brightness in areas of the scene (Fig. 12) represents the additive effect (Band 13 + Band 12 + Band 10) of high emissivity in each band region. It is difficult, if not impossible, to visually differentiate

between different intensity levels in the TIR composite (Fig. 12) because the data in each channel are very strongly correlated. To discriminate or enhance the intensity contrast of the pixels in any composite, mathematical transformations can be applied to the data to subdue the visual effect of temperature variations in the scene and exaggerate those that result from emissivity (Adams and Gillespie, 2005). These transformations are decorrelation functions that filter and transform pixels to aid visual interpretations.

First, an intensity transform, also referred to as an equalization stretch, is applied (Fig. 13) to the TIR composite (Fig. 12). Essentially, the equalization method uses a technique that stretches the small intensity contrasts between pixels in the scene to enhance the emissivity information in the image. In ENVI (ITT-VIS, 2006), the equalization stretch is also referred to as a histogram stretch because this image enhancement procedure is based on the AST_L1B histograms of each band. A number of output bins is used to redistribute the data such that approximately equal number of pixels fall into each bin. To do this, ENVI scales the floating point values to DN values and then uses all 256 DN values (0-255) as bins, followed by the reassignment of near-equal numbers of pixels into each bin (ITT-VIS, 2006). In the output display (Fig. 13), the result of the transformation can be interpreted as color describing the decorrelated emissivity information, and brightness describing the thermal effects.

Next, using a color transform, also referred to as a saturation stretch, another decorrelation function is applied to the TIR composite (Fig. 14). Essentially, the ENVI saturation stretch uses a technique that transforms or stretches the RGB color space to another. A color space is typically used to standardize color descriptions and is best exemplified by the Munsell color system used by soil scientists and geologists to describe

the color of soils and rocks (ITT-VIS, 2006). Examples of types of color space are: the (1) hue, saturation, value (HSV) (more common as HIS; value V is interchanged with intensity, I); (2) hue, lightness, saturation (HLS); or (3) USGS Munsell HSV (ITT-VIS, 2006). In ENVI (ITT-VIS, 2006), the saturation stretch applied to the TIR composite (equalization stretched) is displayed in the HSV color space (Fig. 14), where the resultant image further enhances the emissivity information through the saturation (S) of the image colors and the reduction of the intensity (I) from the thermal effects.

This application of the composite of ASTER TIR Bands 13 (10.25-10.95 μm), 12 (8.925-9.275 μm), and 10 (8.125-8.475 μm), using image post-processing decorrelation methods closely matches the results of Kahle and Rowan (1980) who used the Bendix MIR Band 17 (8.27-8.8 μm), 18 (8.8-9.3 μm), and 20 (10.1-11.0 μm) composite together with image post-processing enhancements (Abrams, 2007). In addition to sampling the same bandwidths, the RGB assignments to the ASTER TIR and the Bendix MIR bands are the same (Kahle and Rowan, 1980). In their work, Kahle and Rowan (1980) found that established laboratory data (Hunt and Salisbury, 1974; 1975; 1976) matched spectra observed during field checks and that the same lab spectra also matched data measured remotely in an airborne investigation over the East Tintic Mountains of Utah. Specifically, Kahle and Rowan (1980) and Kahle et al. (1980) established that the distinct color boundaries in the resultant (decorrelated) composites corresponded to distinct rock-type boundaries. In addition, these studies showed that: reds are good indicators of silicate content—the more intense and true the red, the higher the silica content; pinks are indicators of silicified areas, sandy limestones, quartz latites, and quartz monzonites; blues indicate latites, monzonites, and some carbonates; purples are clays; and the greens

are carbonates, vegetation, and alluvium (Kahle et al., 1980; Kahle and Rowan, 1980). These results thus provide the basis for interpreting color variations in the stretched TIR image (Fig. 14) in this study.

By applying these methods on the ASTER TIR composite, the uncertainty in geologic composition (and therefore the rigidity) of the terrain units can be significantly reduced. For example, the location of the blue and green color-coded regions in the TIR composite (Fig. 14) indicates carbonate rocks (high rigidity) that coincide with the high relief features in the Margala Hills and the linear ridges. The red and pink color-coded regions indicate silicic deposits in intermediate to low relief terrains that are common materials for piedmonts and basins in the study area. For verification purposes, these rock types, derived from the enhanced TIR composite are compared and found to match the independent results of Williams et al. (1999), Zulfiqar et al. (2005) and Munir and Butt (2007) that describe the local geology of the Islamabad region.

Assignment of Shear-wave Velocity Ranges

At a meso-scale (coarse) resolution and for a first-approximation, the Vs30-lithology correlations of Wills et al. (2000) and Wills and Clahan (2006) can be used for site characterization of expected shear-wave velocities in the near surface. In the Wills et al. (2000) study, the characterization of site conditions were expanded statewide by the assignment of shear-wave velocities to sites where *in situ* measurements are not available. These assignments were based on the geologic similarities to sites with measurements. For hard rock sites, Wills et al. (2000) expected the predicted Vs value to be greater than 500 m/s, which is observed mostly in rocks, such as granites, typical of mountain sites in southern California, and as well as in the more consolidated

sedimentary rocks, such as carbonates. Because most mountain features are composed of hard rock with expected velocities equal to or greater than 500 m/s and have a characteristically steep topographic profile, the mountain units are assigned the high portion of the velocity range. For the predicted V_s values in the intermediate category, a large range, 200-600 m/s, was assigned to the moderately sloped piedmont units to account for the high variation in velocities that were predicted for similar terrains observed by Wills and Clahan (2006). Lastly, for the soft rock sites, generally correlated to the relatively flat relief of the terrain, the lowest velocity values are assigned.

The integrated geomorphic (DEM-based) and geologic (spectral-based) classification map is shown (Fig. 15). Mountain areas are shown to be primarily consisting of limestone (hard) rocks and basins to be dominated by silicic (intermediate-soft) rocks. The Wills and Clahan (2006) method described above is then used to assign shear-wave velocity ranges.

SUMMARY AND CONCLUSIONS

Site factor is a critical parameter for describing the predicted ground motion intensity during an earthquake. The site factor, or site condition, affects the response of the ground to seismic disturbances and site effect is the characteristic response of the site to the disturbance. Although, there are many local influences that affect site conditions, the effects of surface geology (ESG) is just one of many important and well-established site factors (for example, Borcherdt, 1970; Fumal and Tinsley, 1978; Aki, 1988; Wills et al., 2000; Wills and Clahan, 2006).

To account for the ESG, information about local geomorphic and geologic site conditions are considered, and then to identify these conditions, precise and consistent

physiographic and lithologic information are used. To extract this information, a systematic and integrated data extraction approach is implemented. On the basis of these considerations, this project develops and applies automated digital imaging analysis methods by integrating pixel-based and object-oriented methods on ASTER satellite imagery to characterize seismic site effects based on the interpretations of geomorphologic and geologic features in the Islamabad, Pakistan region.

To meet the need for precise and consistent geomorphic and the geologic information, ASTER imagery with high spatial and spectral resolutions are used in this project. In addition, the satellite-based system was specifically designed for remote geologic interpretations (Abrams and Hook, 1995; Abrams, 2000) and is the only scientifically accessible system in current operation which includes sensors that record high quality stereocorrelated imagery for generating DEMs on demand (Hirano et al., 2003). The ASTER spatial resolution, at the 15 m (VNIR), 30 m (MIR) and 90 m (TIR) resolutions, and spectral sensitivities, in 14 discrete bands from the 0.52-11.65 μm wavelength region, provides a high resolution (30 m) DEM and spectral scale (1:50,000), that fulfills the requirements for precise map information. In addition, the global coverage of the ASTER imagery provides a set of consistent map information that is beyond the region wide coverage requirement for assessing seismic site conditions.

To accurately interpret and extract geomorphic (terrain-types) and the geologic (rock-types) features, a systematic and integrated approach is implemented. Using commercial digital imaging analysis applications, such as the object-based eCognition program and the pixel-based ENVI program, the project integrated the feature extraction

processes from each program to effectively extract geomorphic and geologic features, which as a set of related factors, control the level of shaking at site-specific locations.

In eCognition, using the ASTER stereocorrelated DEMs (AST14DEM), geomorphic terrain units (mountains, piedmonts, and basins) are extracted and assigned based on the application of the multi-resolution (object-oriented) segmentation method and the nearest neighbor (NN) statistics. First, by applying the object-oriented digital imaging analysis method on the groups of pixels (object primitives) (Fig. 10) that collectively define each terrain unit, prominent mountain and ridge features, including the Margala Hills and the northeast trending linear ridges (Fig. 15), are extracted. Also extracted are remaining features, such as the piedmont benches and the basins. Then, by sampling the representative object primitives, the terrain features in the ASTER imagery are classified (Fig. 15) according to the pre-established definition of a mountain, piedmont or basin unit. To reduce the uncertainty about the rigidity of the terrain units, the composition (geology) of the units are used.

In ENVI, the distribution of the geologic units in the ASTER spectral imagery (AST_L1B) is discriminated based on the Kahle and Rowan (1980) absolute band composition (TIR composite) and digital imaging enhancement methods (pixel-based image decorrelation and saturation). By applying these methods on the ASTER TIR composite, uncertainties about the geologic composition (rigidity) of the terrain units are significantly reduced. The location of the blue and green color-coded regions in the TIR composite (Fig. 14) indicates carbonate rocks (high rigidity) that coincides with the high relief features in the Margala Hills and the linear ridges. Also, the red and pink color-coded regions indicate silicic deposits in intermediate to low relief terrains that are

common characteristics of piedmonts and basins. These rock types, derived from the enhanced TIR composite are compared and found to match the independent results of Williams et al. (1999), Zulfiqar et al. (2005) and Munir and Butt (2007) that describe the local geology of the Islamabad region.

The geologic site conditions are systematically assigned the associated shear-wave velocity ranges after verification that the terrain units match the expected rock types for correlation to compositional rigidity and the typical shear-wave velocities (Wills and Clahan, 2006). In the resultant map, the high relief and limestone regions of the Margala Hills (Fig. 14 and 15) are assigned the highest velocity range (>500 m/s), the Islamabad and Rawalpindi region (piedmont bench), just south of the Margala Hills, are assigned with the intermediate velocity range and the highest variations in velocities (200-600 m/s) (Fig. 15), and the basin, south of the cities, are assigned with the lowest velocity range (< 300 m/s) (Fig. 15).

As a final result, the map, based on local geomorphology and geology, interpreted from the ASTER imagery, is a credible, first-approximation of potential site amplification in the Islamabad study area. There are a few advantages and disadvantages to the approach applied in this project. The approach applied in this project has advantages over other approaches used by recent studies (for example, Romero and Rix, 2001; Wald and Allen, 2007). By using high spatial and spectral resolution imagery and coupling the geomorphic and geologic properties of landform features, the integrated approach provides improved resolution of the spatial and spectral extent and the compositional hardness (rigidity) of features. Also, by using ASTER imagery, this technique can be implemented anywhere because ASTER provides complete global

coverage. In contrast, a seismic study by Romero and Rix (2001) used satellite imagery with lower spectral resolution (6 bands) from the Landsat 7 ETM (Enhanced Thematic Mapper). The smaller number of channels in the Landsat 7 ETM imagery, particularly in the SWIR and TIR, reduces its utility because these channels are crucial for identifying complex rock-types in seismically active terrains. In a more recent study, Wald and Allen (2007) used DEMs that have lower spatial resolution (90 m). The DEMs were based on Synthetic Aperture Radar (SAR) technology from the Shuttle Radar Terrain Mission (SRTM). SAR-based DEMs from the SRTM cannot map latitudes north of 60° , which coincide with the seismically active regions of Alaska, and south of -59° , and it also cannot map steep areas, which are prominent in most active tectonic terrains.

One disadvantage of the integrated approach is encountered when analyzing large regions at a time. The issue is effectively a geometric problem related to the irregular shape of the Earth's surface and the accuracy in the representation of the Earth's curvature over a large region. Although the solution to the problem is not insurmountable, it requires the use of complex and powerful algorithms to accurately produce spatially extensive DEMs. When fine scale spatial accuracy is not required, the Wald and Allen (2007) approach is more appropriate in characterizing seismic hazards at the continental scale. Another disadvantage of this project's approach is that whereas Wald and Allen (2007) can quickly generate a site conditions map by calculating only one parameter (slope) from readily available SRTM DEMs, in the approach described here, both geomorphology and geology, in addition to other preprocesses, are required to prepare the imagery for analysis.

Finally, an evaluation of the resultant map is necessary to determine how well it performs against other approaches. To quantify the map's performance, a comparison of the predicted site conditions from the resultant map against measured amplitude data from a network of seismic recordings is necessary. Recorded ground motions from the 2005 M7.6 Muzaffarabad earthquake would provide independent estimation of amplification factors. These data have not yet been made available to the international community.

REFERENCES CITED

- Abrahamson, N. A., and Silva, W. J., 1997, Empirical response spectral attenuation relations for shallow crustal earthquakes: *Seismological Research Letters*, v. 68, no. 1, p. 94-127.
- Abrams, M., 2000, The advanced spaceborne thermal emission and reflectance radiometer (ASTER): Data products for the high spatial resolution imager on NASA's Terra platform: *International Journal of Remote Sensing*, v. 21, p. 847-859.
- Abrams, M., Hook, S., and Ramachandran, B., 2002, *ASTER User Handbook*: Pasadena, Jet Propulsion Laboratory/California Institute of Technology, 135 p.
- Abrams, M., and Hook, S. J., 1995, Simulated Aster data for geologic studies: *IEEE Transactions on Geoscience and Remote Sensing*, v. 33, no. 3, p. 692-699.
- Abrams, M. J., 2007, Personal communications.
- Adams, J. B., and Gillespie, A. R., 2005, *Remote Sensing of Landscapes with Spectral Images; A Physical Modeling Approach*: Cambridge, University Press, 362 p.
- Agarkov, A. V., Makarov, A. L., Matvienko, S. A., and Meleshko, A. V., 2005, Geophysical parameters-based space system of Earth remote diagnosis, 31st ISRSE Symposium, June 20-24: Saint Petersburg.
- Aki, K., 1988, Local site effects on strong ground motion, *in Earthquake Engineering and Soil Dynamics II - Recent Advances in Ground Motion Evaluation*, ASCE, p. 103-155.
- Anderson, J. G., Lee, Y., Zeng, Y., and Day, S., 1996, Control of strong motion by the upper 30 meters: *Bulletin Seismological Society of America*, v. 86, no. 6, p. 1749-1759.
- Argialas, D., and Tzotsos, A., 2006, Automatic extraction of physiographic features and alluvial fans in Nevada, USA from digital elevation models and satellite imagery through multiresolution segmentation and object-oriented classification, ASPRS 2006 Annual Conference, May 1-5: Reno, Nevada.

- Bard, P. Y., and Bouchon, M., 1980, The seismic response of sediment-filled valleys. Part 1. The case of incident SH waves: *Bulletin Seismological Society of America*, v. 70, no. 4, p. 1263-1286.
- Bard, P. Y., and Gabriel, J. C., 1986, The seismic response of two-dimensional sedimentary deposits with large vertical velocity gradients: *Bulletin Seismological Society of America*, v. 76, no. 2, p. 343-346.
- Bard, P. Y., and Tucker, B. E., 1985, Underground and ridge site effects: A comparison of observation and theory: *Bulletin Seismological Society of America*, v. 75, no. 4, p. 905-922.
- Bolongaro-Crevenna, A., Torres-Rodri'guez, V., Sorani, V., Frame, D., and Ortiz, M. A., 2005, Geomorphometric analysis for characterizing landforms in Morelos State, Mexico: *Geomorphology*, v. 67, p. 407-422.
- Boore, D. M., and Joyner, W. B., 1997, Site amplification for generic rock sites: *Bulletin Seismological Society of America*, v. 87, no. 2, p. 327-341.
- Boore, D. M., Joyner, W. B., and Fumal, T. E., 1997, Equations for estimating horizontal response spectra and peak acceleration from western North American earthquakes: a summary of recent work: *Seismological Research Letters*, v. 68, no. 1, p. 128-153.
- Borcherdt, R. D., 1970, Effects of local geology on ground motion near San Francisco Bay: *Bulletin Seismological Society of America*, v. 60, no. 1, p. 29-61.
- Borcherdt, R. D., 1985, Predicting earthquake ground motions: An introduction: U.S. Geological Survey Professional Paper 1360, 93-100 p.
- Campbell, K. W., 1997, Empirical near-source attenuation relationships for horizontal and vertical components of peak ground acceleration, peak ground velocity, and pseudo-absolute acceleration response spectra: *Seismological Research Letters*, v. 68, no. 1, p. 154-179.
- Campbell, K. W., 2003, Engineering models of strong ground motion, *in* Chen, W. F., and Scawthorn, C., eds., *Earthquake Engineering Handbook*: Boca Raton, CRC Press.

- Clark, P. J., and Evans, F. C., 1954, Distance to nearest neighbor as a measure of spatial relations in populations: *Ecology*, v. 35, p. 445-453.
- Crowley, J. K., Brickley, D. W., and Rowan, L. C., 1989, Airborne imaging spectrometer data of the Ruby Mountains, Montana: Mineral discrimination using relative absorption band-depth images: *Remote Sensing of the Environment*, v. 29, p. 121-134.
- Definiens, T. I. I. C., 2006, *Definiens Professional 5 Basic Training Material*: Munchen, Definiens AG, 69 p.
- Elachi, C., and van Zyl, J. J., 2006, *Introduction to the Physics and Techniques of Remote Sensing*, Wiley Series in Remote Sensing and Image Processing: Hoboken, Wiley-Interscience, John Wiley and Sons, Inc., 584 p.
- Faccioli, E., 1991, Seismic amplification in the presence of geological and topographic irregularities, *in* 2nd International Conference on Recent Advances in Geotechnical Earthquake Engineering and Soil Dynamics, St. Louis, MO, p. 1779-1797.
- Field, E. H., and Petersen, M. D., 2000, A test of various site-effect parameterizations in probabilistic seismic hazard analyses of southern California: *Bulletin Seismological Society of America*, v. 90, no. 6B, p. S222-S244.
- Fumal, T. E., 1978, Correlations between seismic wave velocities and physical properties of near-surface geologic materials in the southern San Francisco Bay region, California: U.S. Geological Survey Open File Report 1067, 114 p.
- Fumal, T. E., and Tinsley, J. C., 1985, Mapping shear-wave velocities of near-surface geologic materials: U.S. Geological Survey Professional Paper 1360, 127-149 p.
- Geli, L., Bard, P., and Jullien, B., 1988, The effects of topography on earthquake ground motion: A review and new results: *Bulletin Seismological Society of America*, v. 78, no. 1, p. 42-63.
- Gueguen, Y., and Palciauskas, V., 1994, *Introduction to the Physics of Rocks*: Princeton, Princeton University Press, 294 p.

- Hirano, A., Welch, R., and Lang, H., 2003, Mapping from ASTER stereo image data: DEM validation and accuracy assessment: Photogrammetry and Remote Sensing, v. 57, p. 356-370.
- Hunt, G. R., and Salisbury, J. W., 1974, Mid-infrared spectral behavior of igneous rocks: U.S. Air Force Cambridge Research Laboratories Technical Report AFCRL-TR-74-0625
- Hunt, G. R., and Salisbury, J. W., 1975, Mid-infrared spectral behavior of sedimentary rocks: U.S. Air Force Cambridge Research Laboratories Technical Report AFCRL-TR-75-0356
- Hunt, G. R., and Salisbury, J. W., 1976, Mid-infrared spectral behavior of metamorphic rocks: U.S. Air Force Cambridge Research Laboratories Technical Report AFCRL-TR-76-0003
- ITT-VIS, 2006, Spectral Analysis With ENVI: Boulder, ITT Visual Information Solutions Global Services, 123 p.
- Kahle, A. B., Madura, D. P., and Soha, J. M., 1980, Middle infrared multispectral aircraft scanner data: analysis for geologic applications: Applied Optics, v. 19, no. 14, p. 2279-2290.
- Kahle, A. B., and Rowan, L. C., 1980, Evaluation of multispectral middle infrared aircraft images for lithologic mapping in the East Tintic Mountains, Utah: Geology, v. 8, p. 234-239.
- Kawase, H., 2003, Site effects on strong ground motions, *in* Lee, W. H., Kanamori, H., Jennings, P. C., and Kissinger, C., eds., International Handbook of Earthquake and Engineering Seismology: International Geophysics Series: Oxford, Academic Press, p. 1013-1030.
- Munir, M., and Butt, A. A., 2007, The paleogene of Azad Kashmir, Hazara Kashmir syntaxis, Pakistan, *in* Geophysical Research Abstracts of 2007 European Geosciences Union, Volume 9-11052, April 15-20, Vienna, Austria.
- Navulur, K., 2006, Multispectral image analysis using the object-oriented paradigm: Boca Raton, CRC Press, 165 p.

- NEIC, 2005, News release: Magnitude 7.6 Pakistan; Saturday, October 08, 2005 at 03:50:40 UTC; preliminary earthquake report, http://neic.usgs.gov/neis/eq_depot/2005/eq_051008_dyae/neic_dyae_nr.html, April 25, 2007.
- Ninomiya, Y., Fu, B., and Cudahy, T. J., 2005, Detecting lithology with Advanced Spaceborne Thermal Emission and Reflection Radiometer (ASTER) multispectral thermal infrared "radiance-at-sensor" data: *Remote Sensing of the Environment*, v. 99, p. 127-139.
- Park, S., and Elrick, S., 1998, Predictions of shear-wave velocities in southern California using surface geology: *Bulletin Seismological Society of America*, v. 88, no. 3, p. 677-685.
- Peacock, M. A., 1931, The Modoc Lava field, northern California: *Geographical Review*, v. 21, no. 2, p. 259-275.
- Petersen, M., Bryant, W. A., Cramer, C. H., Reichle, M. S., and Real, C. R., 1997, Seismic ground-motion hazard mapping incorporating site effects for Los Angeles, Orange, and Ventura Counties, California: A geographical information system application: *Bulletin Seismological Society of America*, v. 87, no. 1, p. 249-255.
- Pike, R. J., 2002, A bibliography of terrain modeling (geomorphometry), the quantitative representation of topography — Supplement 4.0: U.S. Geological Survey Open File Report 465, 158 p.
- Press, F., 1966, Seismic velocities, *in* Clark, S. P., ed., *Handbook of Physical Constants*: New York, The Geological Society of America.
- Ray, R. G., 1960, *Aerial Photographs in Geologic Interpretation and Mapping*: U.S. Geological Survey Professional Paper 373, 230 p.
- Reid, H. F., 1910, The California earthquake of April 18, 1906: Carnegie Institute of Washington Publication 87, 451 p.
- Romero, S. M., and Rix, G. J., 2001, Ground motion amplification of soils in the upper Mississippi embayment: National Science Foundation Mid America Earthquake Center Report No. GIT-CEE/GEO-01-1, 461 p.

- Rowan, L. C., Mars, J. C., and Simpson, C. J., 2005, Lithologic mapping of the Mordor, NT, Australia ultramafic complex by using the Advanced Spaceborne Thermal Emission and Reflection Radiometer (ASTER): Remote Sensing of the Environment, v. 99, p. 105-126.
- Rymer, M. J., 1987, The San Salvador earthquake of October 10, 1986—Geologic Aspects: Earthquake Spectra, v. 3, no. 3, p. 435-463.
- Rymer, M. J., 1994, Quaternary fault-normal thrusting in the northwestern Mecca Hills, southern California, *in* Guidebook: Geological Society of America Cordilleran Section Meeting, April 9-11, San Bernardino.
- Sadigh, K., Chang, C. Y., Egan, J. A., Makdisi, F., and Youngs, R. R., 1997, Attenuation relationships for shallow crustal earthquakes based on California strong motion data: Seismological Research Letters, v. 68, no. 1, p. 180-189.
- Sánchez-Sesma, F. J., and Campillo, M., 1993, Topographic effects for incident P, SV and Rayleigh waves: Tectonophysics, v. 218, no. 1-3, p. 113-125.
- Theodoridis, S., and Koutroumbas, K., 2006, Pattern Recognition, Academic Press, 856 p.
- Tinsley, J., Hough, S. E., Yong, A., Kanamori, H., Yu, E., Appel, V., and Wills, C. J., 2004, Geotechnical Characterization of TriNet Sites: A Status Report: Seismological Research Letters, v. 75, no. 2, p. 505.
- Tinsley, J. C., and Fumal, T. E., 1985, Mapping quaternary sedimentary deposits for areal variations in shaking response: U.S. Geological Survey Professional Paper, 101-126 p.
- Wald, D. J., and Allen, T. I., 2007, Topographic slope as a proxy for seismic site condition and amplification, *in* SSA 2007 Annual Meeting, April 11-13, Kona, HI.
- Williams, V. S., 1999, Geologic map of the Islamabad-Rawalpindi area, Punjab, northern Pakistan (map supplement): U.S. Geological Survey Open File Report 47, 16 p.
- Wills, C. J., 2007, Personal Communications.

- Wills, C. J., and Clahan, K. B., 2006, Developing a map of geological defined site-condition categories for California: *Bulletin Seismological Society of America*, v. 96, no. 4A, p. 1483-1501.
- Wills, C. J., Petersen, M., Bryant, W. A., Reichle, M., Saucedo, G. J., Tan, S., Taylor, G., and Treiman, J., 2000, A Site-Conditions map for the California based on geology and shear-wave velocity: *Bulletin Seismological Society of America*, v. 90, no. 6B, p. S187-S208.
- Wills, C. J., and Silva, W., 1998, Shear-wave velocity characteristics of geologic units in California: *Earthquake Spectra*, v. 14, no. 3, p. 533-556.
- Wood, H. O., 1908, Distribution of apparent intensity in San Francisco, in the California earthquake of April 18, 1906: *Carnegie Institute of Washington Report of the State of Earthquake Investigation Commission*, 220-245 p.
- Yamaguchi, Y., Kahle, A. B., Tsu, H., Kawakami, T., and Pniel, M., 1998, Overview of advanced spaceborne thermal emission and reflection radiometer (ASTER): *IEEE Transactions on Geoscience and Remote Sensing*, v. 36, no. 4, p. 1062-1071.
- Yan, G., 2003, Pixel based and object oriented image analysis for coal fire research: *International Institute for Geo-information Science and Earth Observation*, 82 p.
- Yong, A., Hough, S., Wills, C. J., and Abrams, M., 2006a, A report on the geotechnical site characterization efforts in southern California, *in SCEC 2006 Annual Meeting*, September 9-14, Palm Springs.
- Yong, A., Hough, S. E., Cox, H., Tiampo, K., Braverman, A., Harvey, J., Hook, S., Hudnut, K., and Simila, G., 2006b, Balloons to satellites: a century of progress in geotechnical site characterization, *in SSA 2006 Annual Meeting*, San Francisco, CA.
- Yong, A., Hough, S. E., Hudnut, K., Healy, S., Giberson, J., and Simila, G., 2005, Geotechnical site characterization using remote sensing data: A feasibility study, *in SSA 2005 Annual Meeting*, Lake Tahoe, NV.
- Yong, A., Hough, S. E., Wills, C. J., and Abrams, M. J., 2006c, Site Characterization Using Satellite Imagery, *in AGU 2007 Fall Meeting*, San Francisco, CA.

Yong, A., Hough, S. E., Wills, C. J., and Abrams, M. J., 2007, Site characterization using satellite imagery: A progress report, *in* SSA 2007 Annual Meeting, April 11-13, Kona, HI.

Zulfiqar, A., Iftikhar, A., Gulraiz, A., and shazia, A., 2005, Seismotectonics and seismic hazard analysis in selected areas of Margala Hills, Islamabad: *Pakistan Journal of Hydrocarbon Research*, v. 15, p. 65-72.

TABLES

Map Category	Expected V_s Range	Number of Profiles	Mean V_s^{30}	Median V_s^{30}	Standard Deviation
B	>760	7	686	674	275
BC	555–1000	38	724	583	368
C	360–760	42	464	423	147
CD	270–555	154	372	365	98
D	180–360	239	301	281	104
DE	90–270	46	298	222	225
E	<180	15	163	165	31

Table 1. Summary of measured shear-wave velocity for the Wills et al. (2000) statewide site conditions map (after Wills et al., 2000).

Geologic Unit	Geologic Description	No. of profiles	Mean Vs30	S.D.	Vs30 from Mean of In	S.D. of In	Mean of In of Vs30
Qi	Intertidal Mud, including mud around the San Francisco Bay and similar mud in the Sacramento/San Joaquin delta and in Humboldt Bay	20	160	39	155	0.243	5.046
af/qi	Artificial fill over intertidal mud around San Francisco Bay	44	217	94	202	0.357	5.310
Qal, fine	Quaternary (Holocene) alluvium in areas where it is known to be predominantly fine	13	236	55	229	0.238	5.437
Qal, deep	Quaternary (Holocene) alluvium in areas where the alluvium (Holocene and Pleistocene) is more than 30 m thick; generally much more in deep basins	161	280	74	271	0.250	5.604
Qal, deep, Imperial V	Quaternary (Holocene) alluvium in the Imperial Valley, except sites in the northern Coachella Valley adjacent to the mountain front	53	209	31	207	0.135	5.335
Qal, deep, LA Basin	Quaternary (Holocene) alluvium in the Los Angeles basin, except sites adjacent to the mountain fronts	64	281	85	270	0.275	5.599
Qal, thin	Quaternary (Holocene) alluvium in narrow valleys, small basins, and adjacent to the edges of basins where the alluvium would be expected to be underlain by contrasting material within 30 m	65	349	89	338	0.244	5.825
Qal, thin, west LA	Quaternary (Holocene) alluvium in part of west Los Angeles where the Holocene alluvium is known to be thin, and is underlain by Pleistocene alluvium	41	297	45	294	0.150	5.684
Qal, coarse	Quaternary (Holocene) alluvium near fronts of high, steep mountain ranges and in major channels where the alluvium is expected to be coarse	18	354	82	345	0.223	5.845
Qoa	Quaternary (Pleistocene) alluvium	132	387	142	370	0.273	5.916
Qs	Quaternary (Pleistocene) sand deposits, such as the Merritt Sand in the Oakland area	15	302	46	297	0.171	5.697
QT	Quaternary to Tertiary (Pleistocene–Pliocene) alluvial deposits such as the Saugus Formation of southern California, Paso Robles Formation of central coast ranges, and the Santa Clara Formation of the Bay Area.	18	455	150	438	0.266	6.083
Tsh	Tertiary (mostly Miocene and Pliocene) shale and siltstone units such as the Repetto, Fernando, Puente, and Modelo Formations of the Los Angeles area	55	390	112	376	0.272	5.930
Tss	Tertiary (mostly Miocene, Oligocene, and Eocene) sandstone units such as the Topanga Formation in the Los Angeles area and the Butano sandstone in the San Francisco Bay area	24	515	215	477	0.386	6.169
Tv	Tertiary volcanic units including the Conejo Volcanics in the Santa Monica Mountains and the Leona Rhyolite in the East Bay Hills	3	609	155	597	0.240	6.392
Kss	Cretaceous sandstone of the Great Valley Sequence in the central Coast Ranges	6	566	199	539	0.332	6.291
serpentine	Serpentine, generally considered part of the Franciscan complex	6	653	137	641	0.204	6.464
KJf	Franciscan complex rock, including melange, sandstone, shale, chert, and greenstone	32	782	359	712	0.432	6.569
xtaline	Crystalline rocks, including Cretaceous granitic rocks, Jurassic metamorphic rocks, schist, and Precambrian gneiss	28	748	430	660	0.489	6.493

Table 2. Geologic units and shear-wave velocity characteristics for the expanded 19-categories proposed by Wills and Clahan (2006).

FIGURES

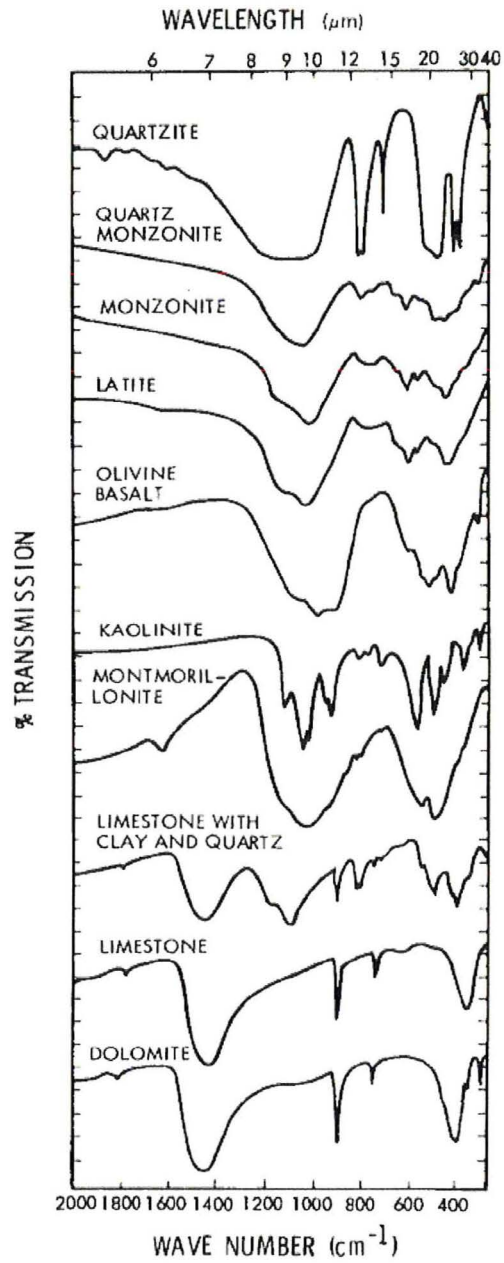


Figure 1. Laboratory transmission spectra of selected rocks and minerals (Kahle and Rowan, 1980; Hunt and Salisbury, 1974; 1975; 1976).

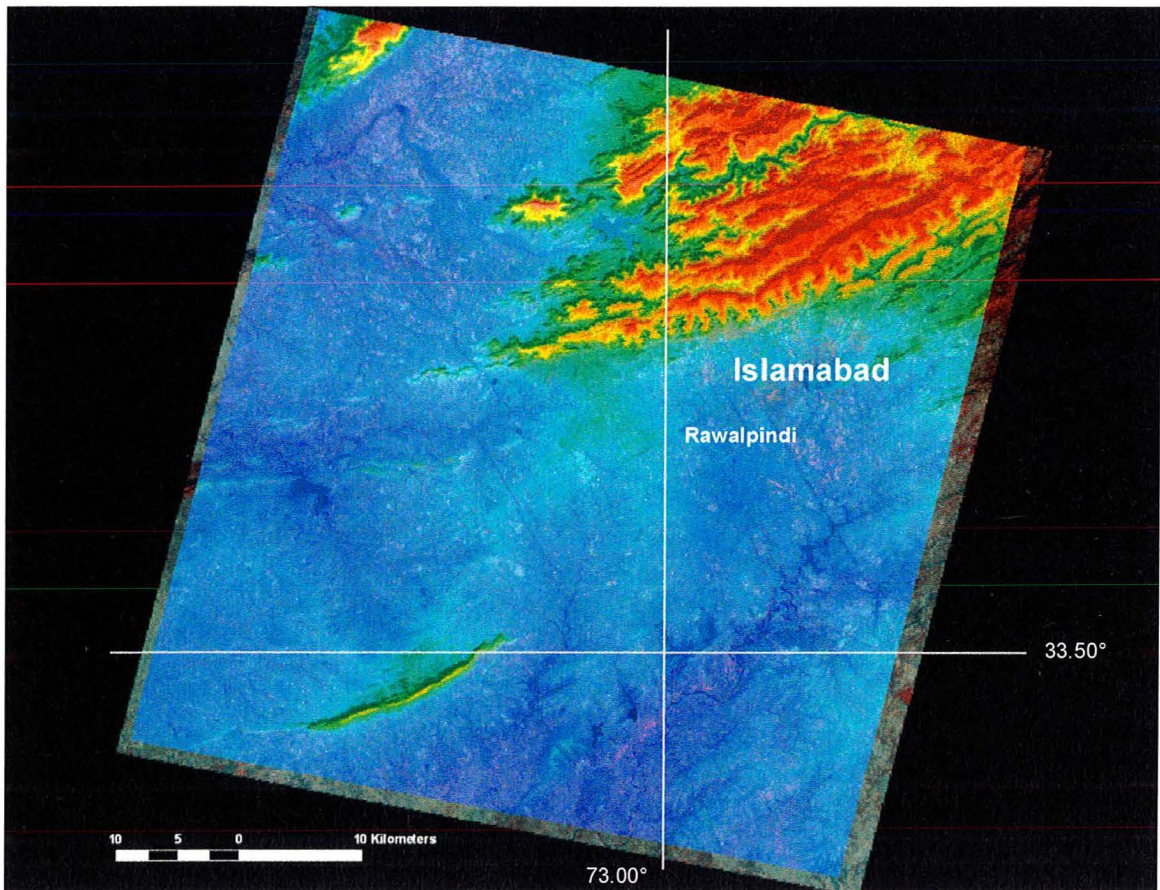


Figure 2. Map of the study area, located near Islamabad and Rawalpindi, in Pakistan. The top image layer (brightly color coded) is the relative DEM (AST14DEM) and the bottom image layer (muted color) is the VNIR composite (AST_L1B).

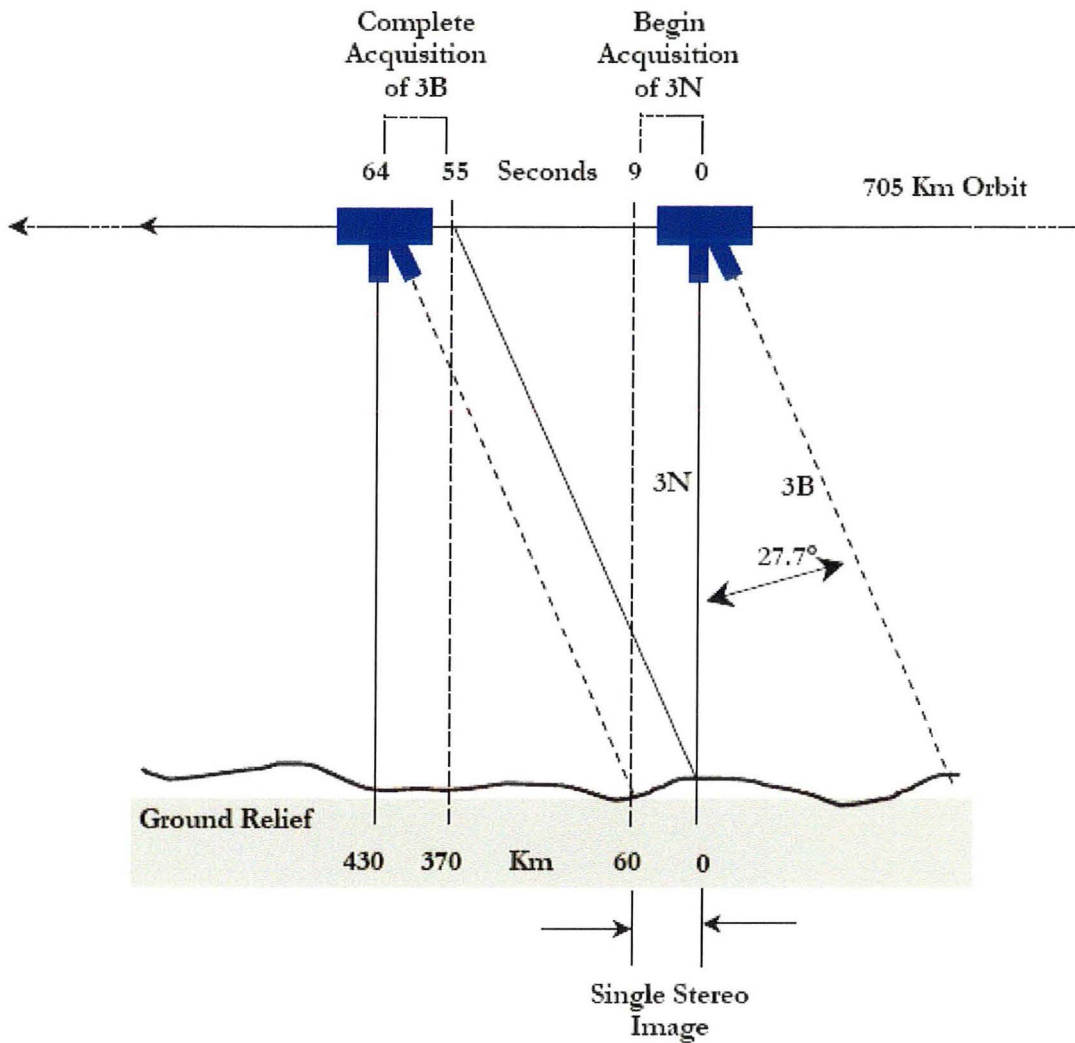


Figure 3. Geometry of the along-track recording mode for the ASTER VNIR nadir (3N) and backward viewing sensors (<http://edcdaac.usgs.gov/aster/ast14dem.asp>).

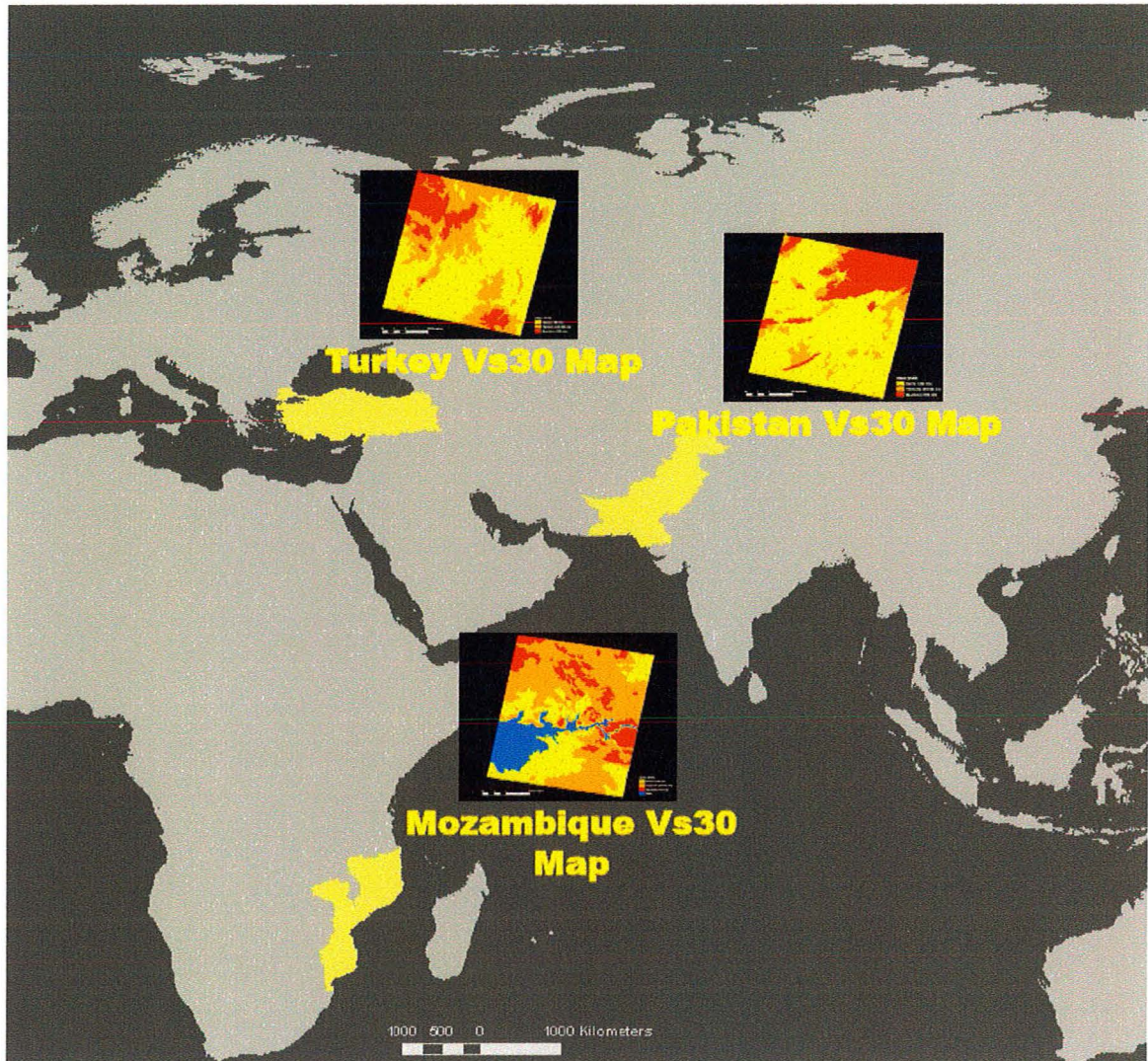


Figure 4. Regional map showing first-order site characterization maps based only on the geomorphology in each region, such as Turkey, Pakistan and Mozambique, which have distinctively different depositional environments (Yong et al., 2006c).

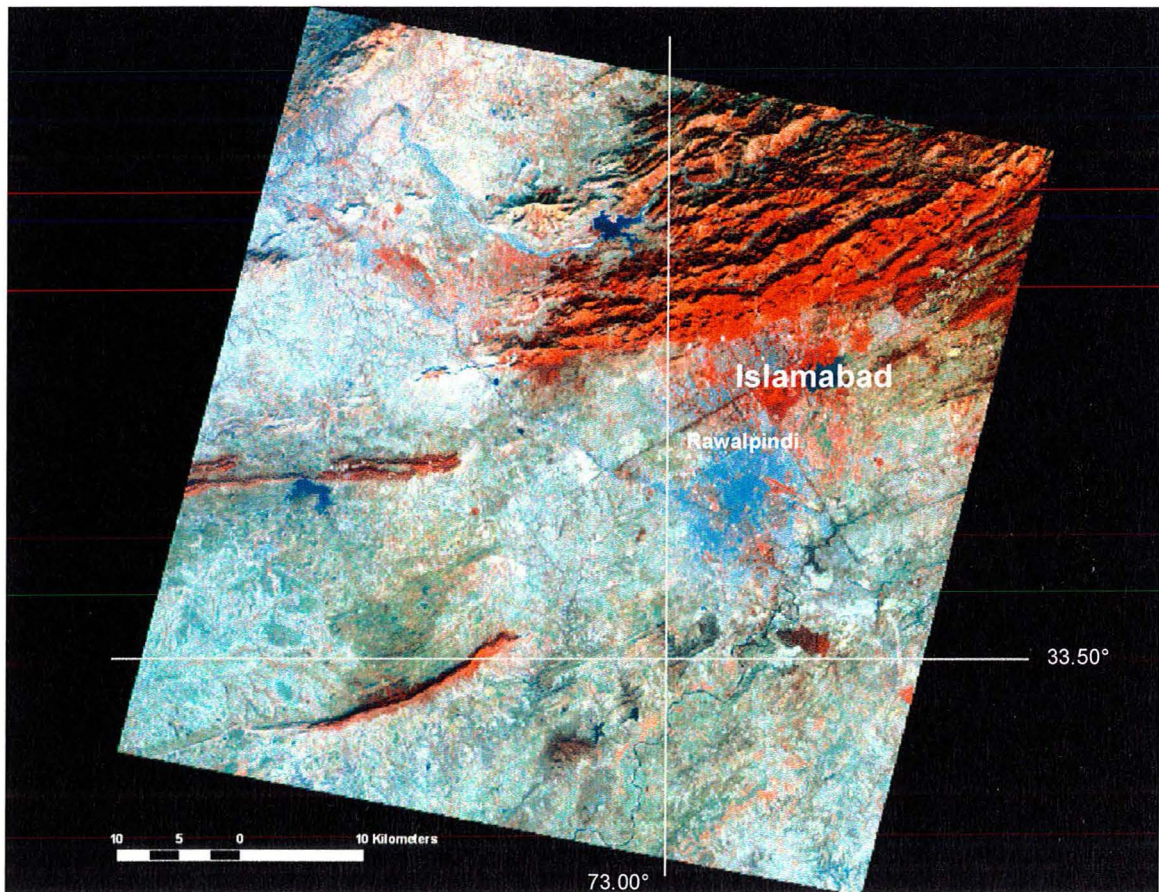


Figure 5. False color ASTER VNIR composite in output space, where Layer 1 (0.52-0.60 μm), Layer 2 (0.63-0.69 μm), and Layer 3N (0.78-0.86 μm) are assigned to the RGB display channels (respectively). Vegetation is displaying the color red.

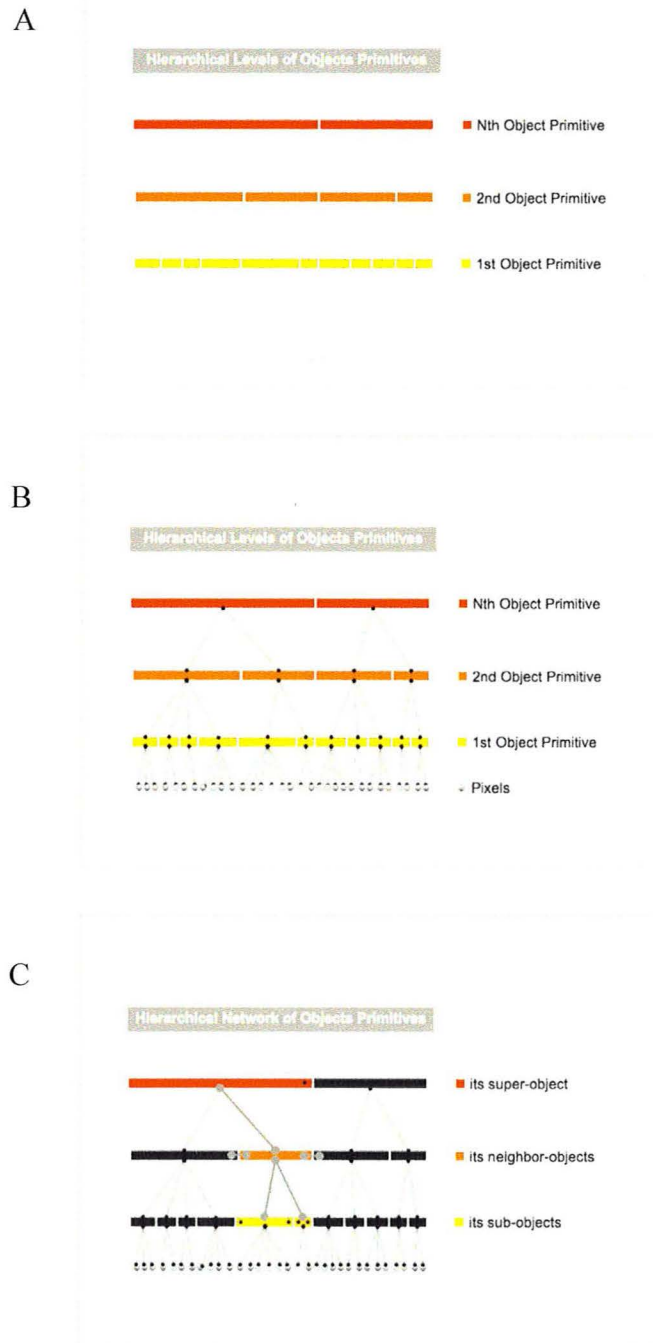


Figure 6. Diagrams (A-C) showing the process for the creation of the hierarchical levels of object primitives (Definiens, 2006). Based on the degree of importance assigned to the contextual information, hierarchical levels (A) of object primitives are created. Through the pair-wise clustering of pixels (B), followed by a bottom-up region-merging technique (B), the segmentation process takes advantage of the resultant hierarchical network of object primitives that is cognizant of its neighbor-objects (C), its sub-objects (C), and its super-objects (C), creating contextual information at multiple scales (Definiens, 2006).

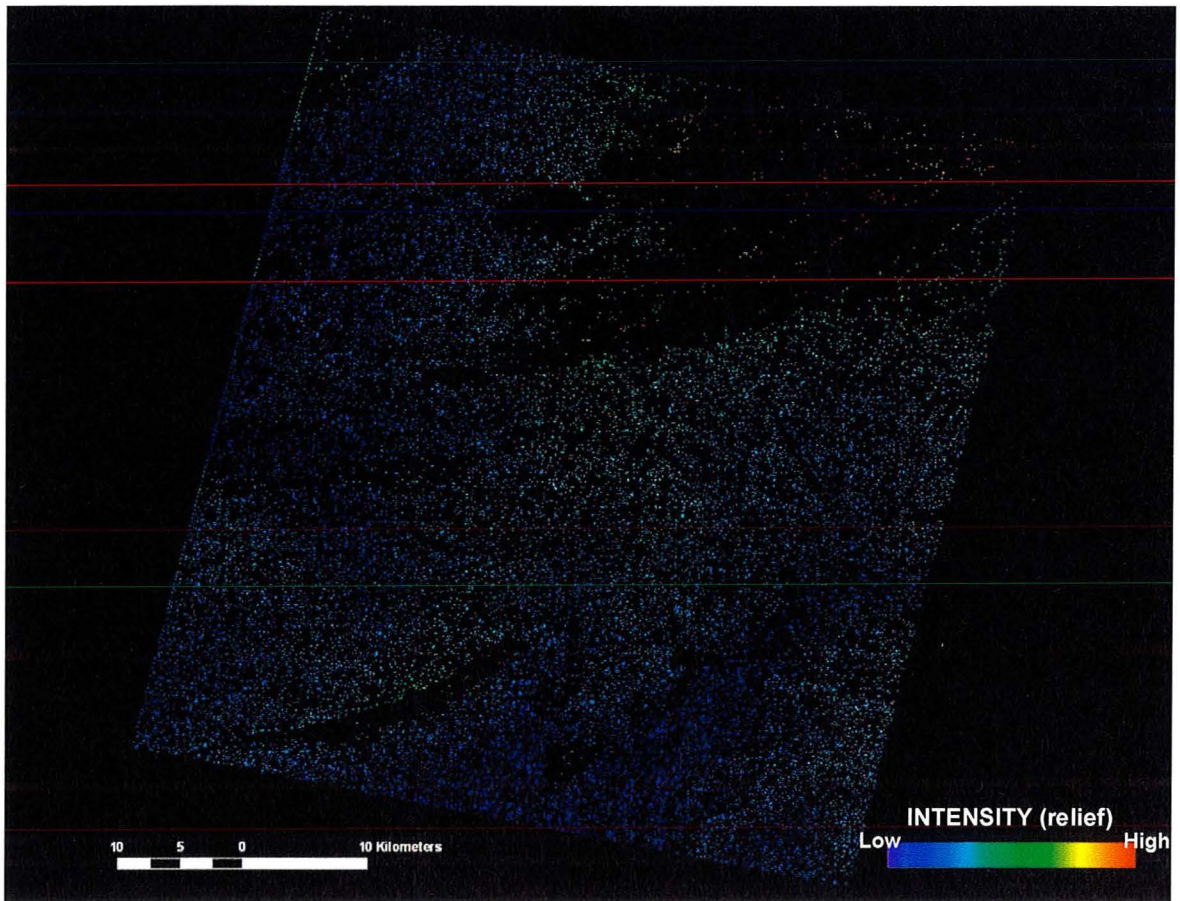


Figure 7. Composite of the first object primitive level and the relative DEM image (Fig. 2) (Yong et al., 2006c). The segmentation results produced a very dense scene filled with small object primitives that outlined the steep relief terrains (dark areas) in the northwest corner, the upper northeast quadrant, and the southwest quadrant.

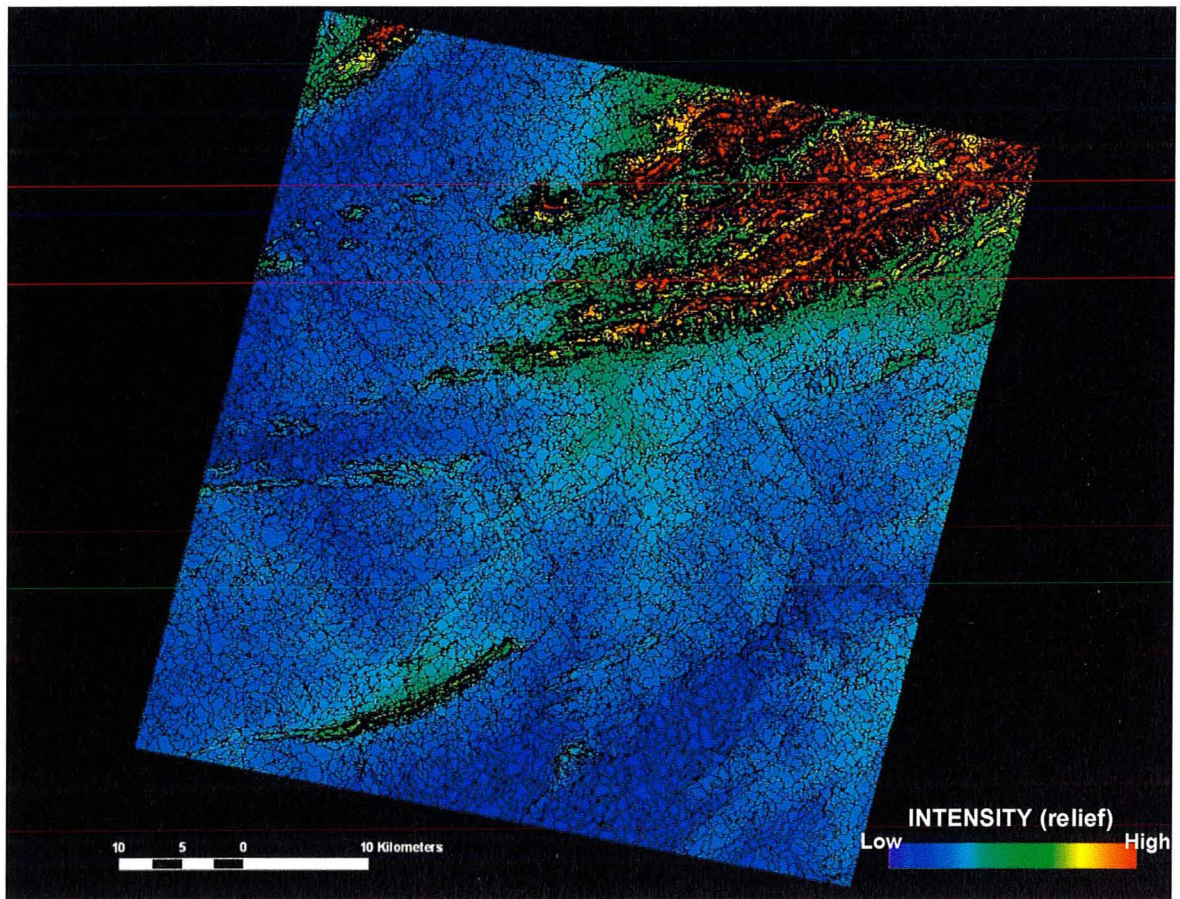


Figure 8. Composite of the second object primitive level and the relative DEM image (Fig. 2) (Yong et al., 2006c). The segmentation results maintain the outline of the steep terrains as characterized by the dark features in the first object primitive level. Other steep terrains, previously not apparent, are now taking shape.

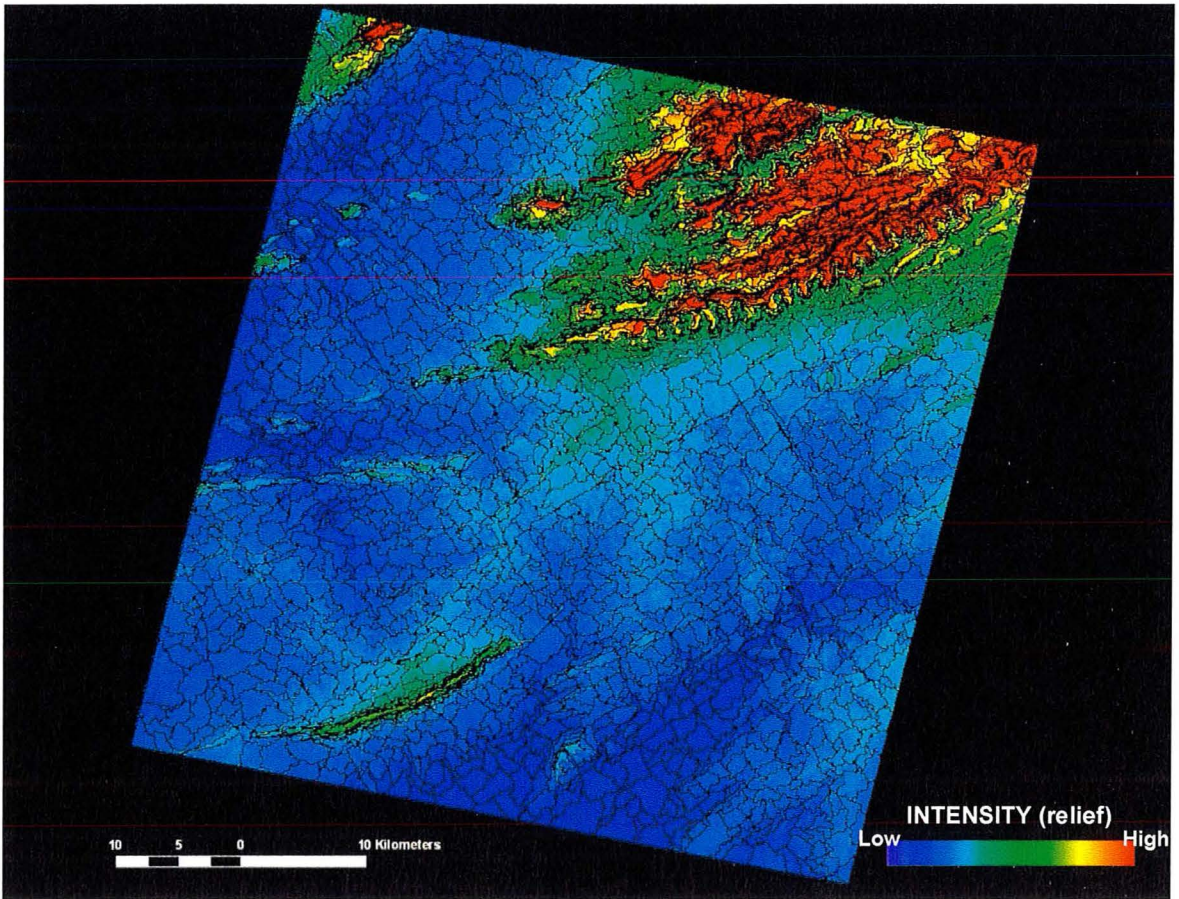


Figure 9. Composite of the third object primitive level and the relative DEM image (Fig. 2) (Yong et al., 2006c). The segmentation results delineate the steep relief terrains (dark areas) in the northwest corner, the upper northeast quadrant, and the southwest quadrant, previously implied in the first object primitive level and have now taken form. Note the ridge, not previously apparent at the top of the southwest quadrant has now also taken form.

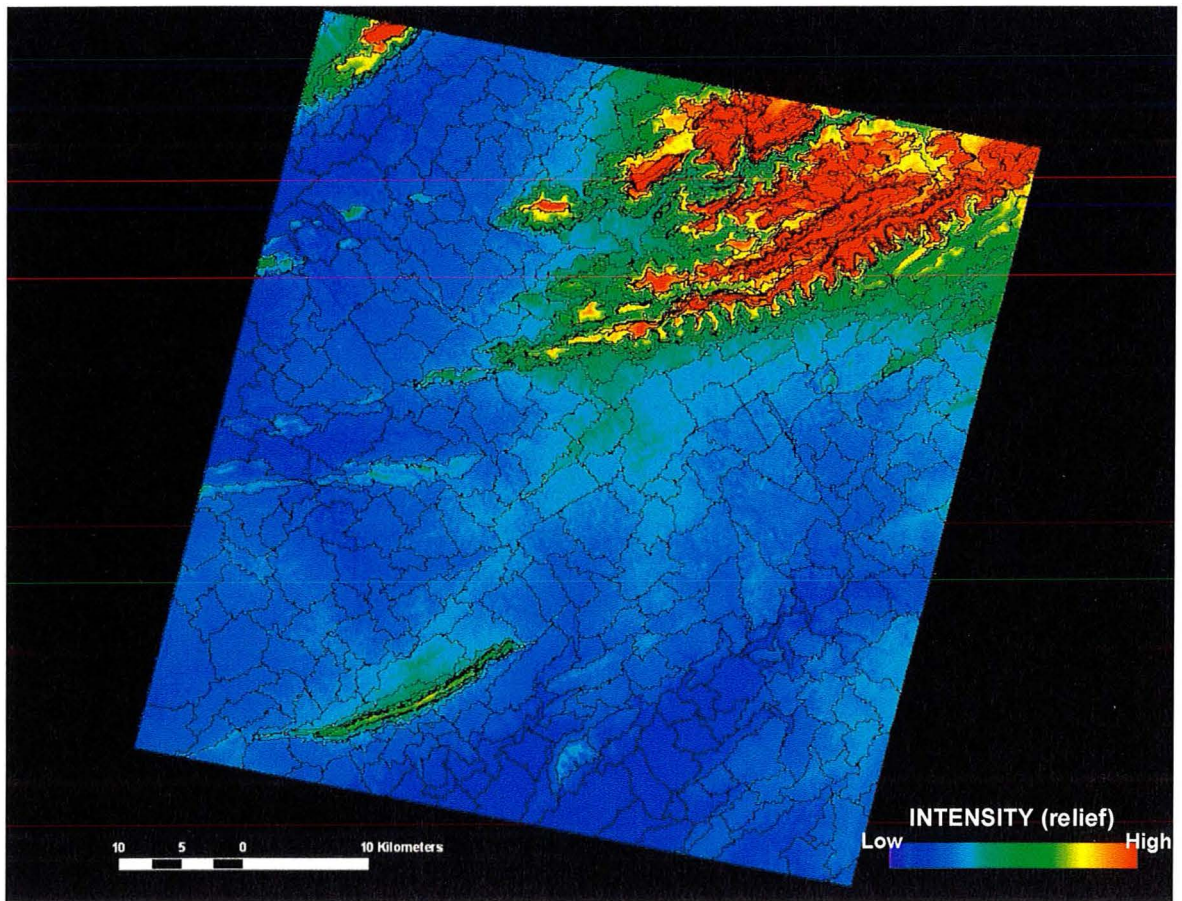


Figure 10. Composite of the fourth and final object primitive level and the relative DEM image (Fig. 2) (Yong et al., 2006c). At this segmentation stage, based on visual comparisons with the relative DEM image, the mountain, piedmont and basin units, represented by the final object primitives, have now finally taken acceptable form.

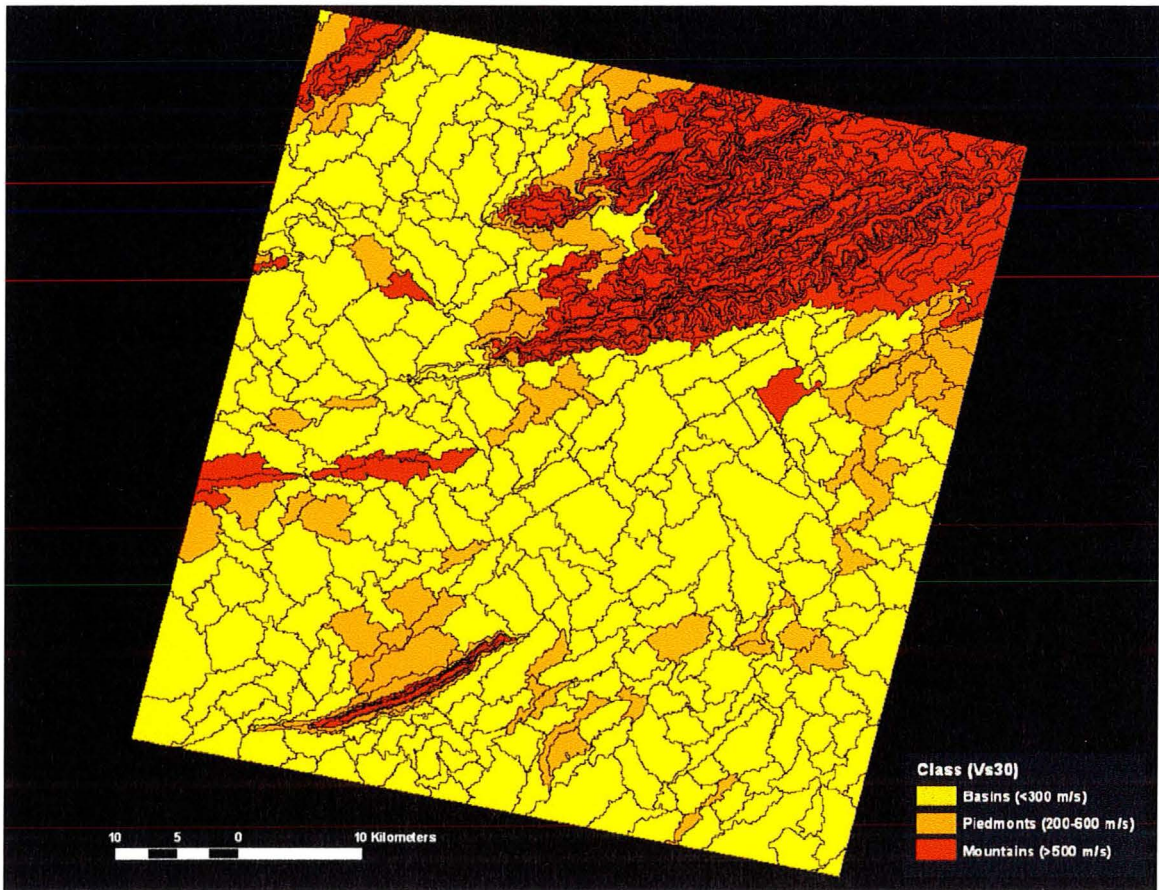


Figure 11. Composite of the fourth and final object primitive level and the result of the NN classification with terrain units and expected Vs30 ranges preliminarily assigned (Yong et al., 2006c).

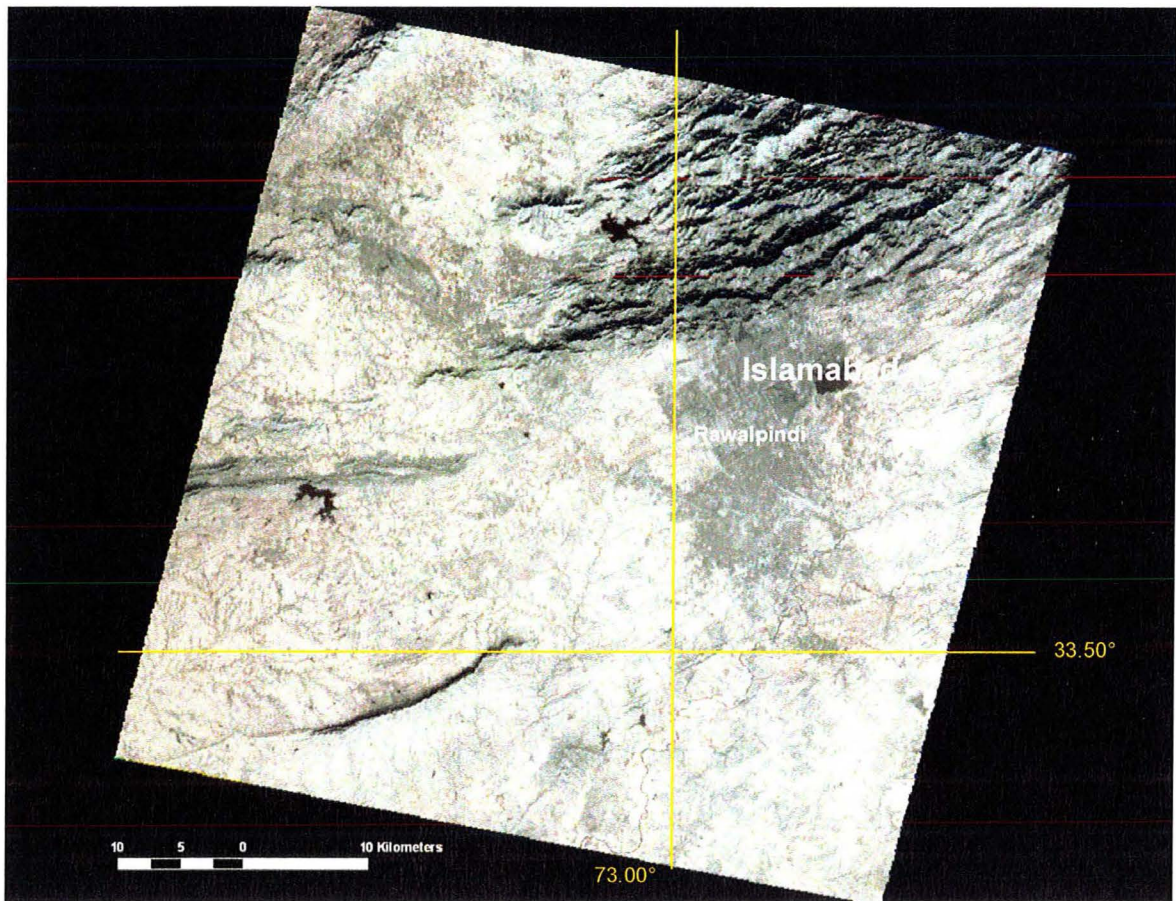


Figure 12. Composite of the ASTER TIR Bands 13 (10.25-10.95 μm), 12 (8.925-9.275 μm), and 10 (8.125-8.475 μm), assigned to display channels R, G and B, respectively (Yong et al., 2007).

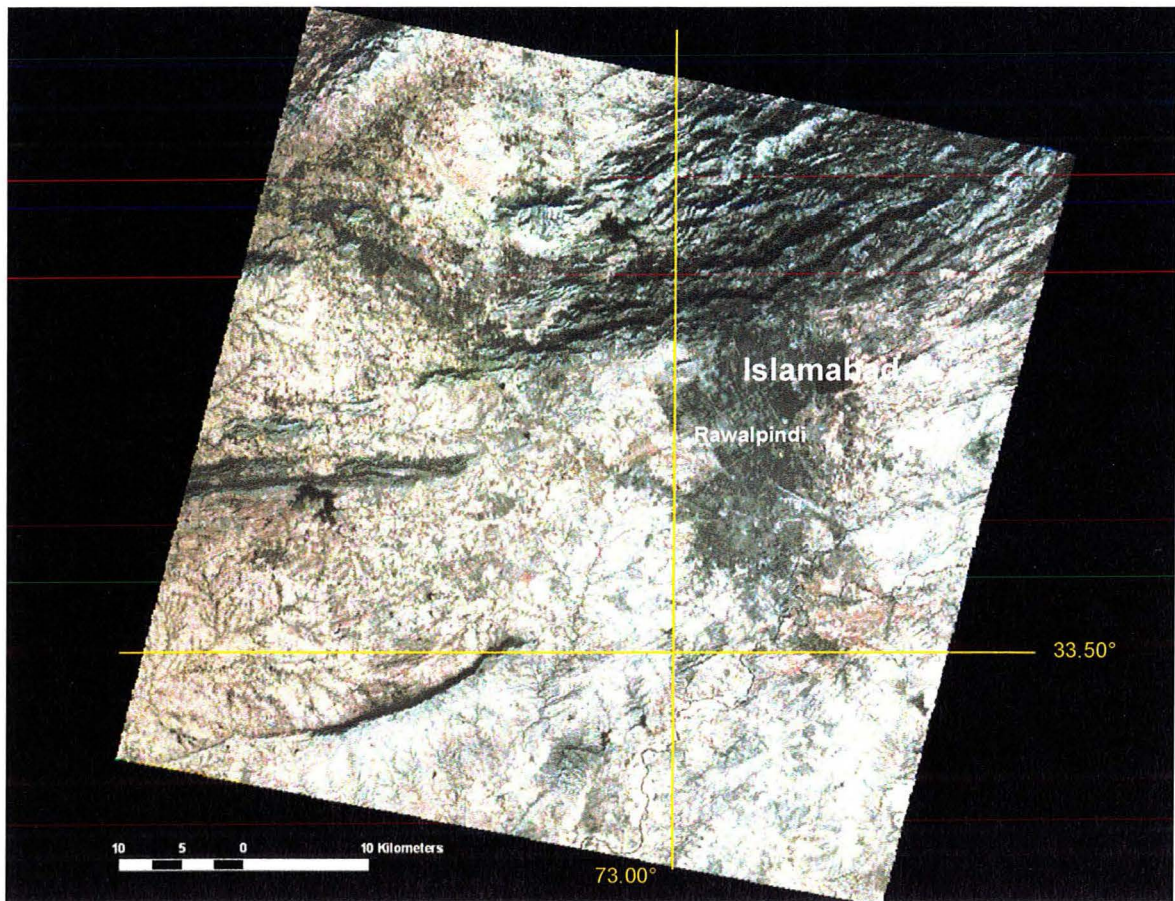


Figure 13. Composite of the ASTER TIR Bands (Fig. 12), after the application of the equalization stretch (Yong et al., 2007).

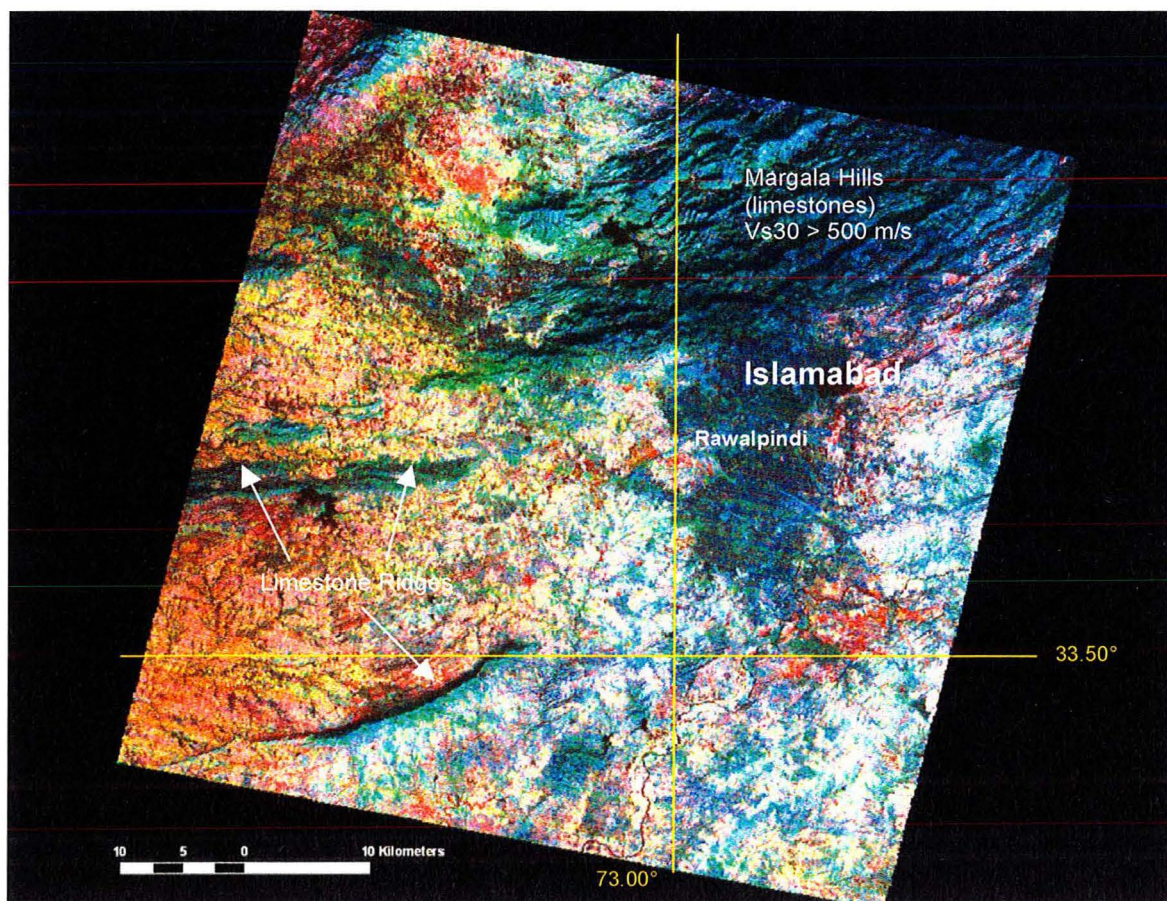


Figure 14. Composite of the stretched (equalization) ASTER TIR Bands (Fig. 13), after the application of the saturation stretch (Yong et al., 2007).

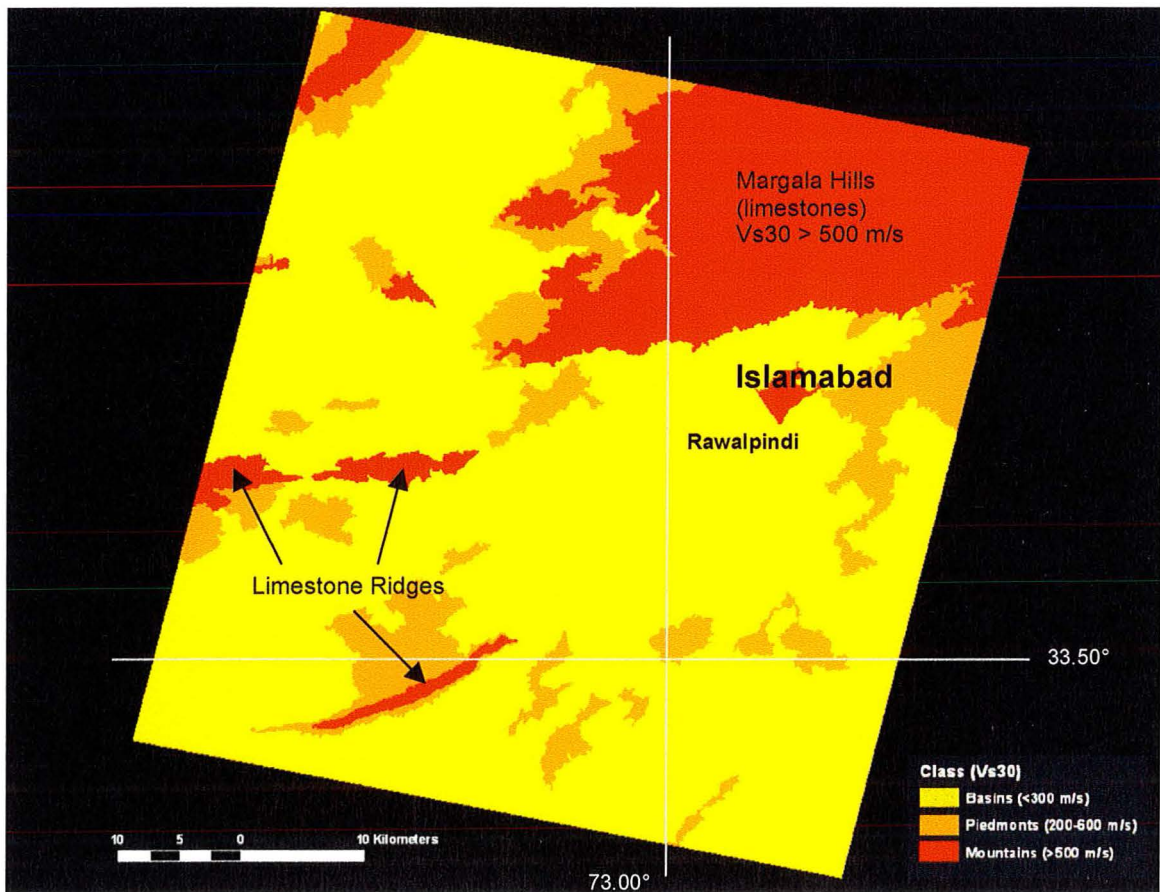


Figure 15. Map of predicted Vs30 (Yong et al., 2006c) with verification of geologic composition based on Williams et al. (1999), Zulfiqar et al. (2005), and, Munir and Butt (2007).

APPENDIX A

Seismic Ground Motions

Propagation and Attenuation of Seismic Waves The propagation of seismic disturbances through the Earth is affected by the physical material properties and the response of the Earth to the disturbance. Furthermore, these materials are compositionally heterogeneous, which adds to the complexity in describing the actual behavior of seismic waves as they propagate from the earthquake source. In order to adequately describe the propagation of seismic waves, simplified assumptions, such as the approximation of real conditions, are used. For example, an important assumption is that seismic energy travels by elastic displacements of the materials in the medium and that the further the seismic energy travels away from the earthquake source, the weaker it becomes (Lowrie, 1997). The former effect is based on the elasticity theory and the latter is referred to as attenuation, where the amplitude of the observed seismic wave decreases with increase distance from the earthquake source.

One important cause of attenuation is energy loss due to the geometric spreading of the seismic wave as it travels outward from the earthquake source. Another is through the absorption of energy due to the imperfect elastic properties of the materials in the propagation path. To quantitatively describe the ability of the Earth to attenuate the energy of seismic waves, the quality factor Q was adopted by Aki and Richards (1980). Attenuation curves are typically used for the empirical predictions of ground motion in earthquake engineering applications and are strongly related to the Q of the medium along the propagation path. It is in these attenuation relations that site effects play an important role in the prediction of ground motions.

Fundamentally, the reduction of energy in the propagation of seismic waves is affected primarily by geometric attenuation (Lowrie, 1997). When seismic energy is released from the earthquake source, the body waves propagate in an outward direction, while spreading spherically (Lowrie, 1997). At the front of the spherical wave is the surface where all particles vibrate with the same phase (Lowrie, 1997). As the distance between the earthquake source and wave front increases, the curvature of the wave front decreases. At large distances, the wave front is so flat that it is then referred to as a plane wave (Lowrie, 1997). Because there are no increases in the overall energy (first law of thermodynamics), the same amount of energy is evenly distributed over a continually expanding surface such that the intensity of the initial energy (per area) diminishes as the distance from the source increases. Hence, geometric attenuation is given as (Lowrie, 1997):

$$I_b(r) = \frac{E_b}{2\pi r^2},$$

where: I_b describes the intensity of the body waves; r describes the distance of the wave front from the seismic source; and E_b describes the energy per unit area of the wave front.

Attenuation is also affected by the absorption of energy due to the elastic properties of the material in the propagation path (Lowrie, 1997). Here, because of the heterogeneity of the materials, the Earth responds anelastically and fails to completely transfer all of seismic energy from one particle to another. The process where part of the energy lost is referred to as anelastic damping and is converted as internal friction (Lowrie, 1997).

Aki and Richards (1980) applied the dimensionless quantity Q as a means to describe the gross effects of internal friction (also known as intrinsic attenuation) as a

result of anelastic damping. The origin of Q can be traced to electric circuit theory where it is used to describe the performance of oscillatory circuits (Lowrie, 1997). In Aki and Richards (1980), it is given as:

$$\frac{1}{Q(\omega)} = -\frac{\Delta E}{2\pi E},$$

where: ω is a the frequency at which a volume of material is cycled; E describes the peak strain energy stored in the volume; and $-\Delta E$ describes the energy lost in each cycle due to the imperfections in the elasticity of the materials. In order to quantify the effect of damping on the seismic signal, the energy density averaged (I_{ave}) over a harmonic cycle of the seismic disturbance must first be considered (Lowrie, 1997):

$$I_{ave} = \frac{1}{2} \rho \omega^2 A^2,$$

where: ρ is the density of the material during the passage of the wave; ω is the frequency of interest; and A is the amplitude of the wave. Next, the equation for the factor-Q is rewritten as (Lowrie, 1997):

$$\frac{2\pi}{Q} = -\frac{1}{E} \lambda \frac{dE}{dr},$$

where: λ is the wavelength of the seismic wave. Further simplification results in the form:

$$\frac{dE}{E} = -\frac{2\pi}{Q} \frac{dr}{\lambda}$$

Since the average energy (I_{ave}) in a wave is proportional to the square of its amplitude A, the simplified form is rewritten as:

$$\frac{dE}{E} = \frac{2dA}{A}$$

Then, to consider the effect of Q observed in the amplitude (A) of a seismogram, damping is given by (Lowrie, 1997):

$$A = A_0 \exp\left(-\frac{\pi r}{Q\lambda}\right) = A_0 \exp\left(-\frac{r}{D}\right),$$

where: D is the distance where amplitude falls to 1/e (36.8%) or roughly one third of its original value; and the r is the distance from its seismic source. Here, for any given wavelength (λ), D is proportional to the Q-factor for the propagation path, such that a rock with a high Q-factor will not significantly reduce the energy of the seismic wave through anelastic damping while traveling large distances (D) (Lowrie, 1997). For seismic body waves, D is typically of the order of 10,000 km, and, for surface waves, D is about 5000 km (Lowrie, 1997). On the other hand, because the Q-factor for P-waves (Primary waves or compressional waves) are generally higher than for S-waves (Secondary waves or shear-waves), anelastic damping is primarily affected by the shear component of the strain (Lowrie, 1997). Hence, in solids with low rigidity, seismic waves will cause shear strain to reach very high levels and respond with higher damping levels than solids with higher rigidity. The Q-factor is also both frequency-dependent and region dependent, such that higher frequencies are more rapidly attenuated than lower frequencies and Q-factors vary significantly for different tectonic regions (Lowrie, 1997). Q-factor is an important quantity in describing the amplitude in recorded seismograms because it is the basis which anelastic damping or attenuation of seismic energy is accounted for in predicting estimated ground motions.

All attenuation curves or relations are equations that estimate the level of expected ground motions derived from seismic recordings through a statistical fitting procedure called regression analysis. Most ground motion attenuation relations or

models predict the expected ground motion level as a function of magnitude and distance, and, are usually determined in two different, but related approaches: (1) the empirical approach, where large data sets of recorded ground motions are used to estimate expected ground motions; and (2) the theoretical, or numerical modeling approach, where synthetic seismograms are generated from ground motion models that account for source, path, site effects and other complexities (Abrahamson and Shedlock, 1997). Here, an overlap is apparent, since empirical approaches usually fit observed data to a theoretical functional form and theoretical approaches use empirical data to determine some of its parameters (Abrahamson and Shedlock, 1997). For example, it is important to clarify that the Boore et al. (1997), or BJK97, attenuation relations is based on the empirical (statistical) (Campbell, 2003) approach and the Atkinson and Boore (1997) attenuation relations is based on the theoretical (stochastic) (Campbell, 2003) approach. In practice, theoretical approaches are used when there are insufficient recordings of ground motion to apply an empirical approach for predicting an estimated ground motion (Campbell, 2003).

Models based on empirical predictions of ground motion are developed through the observation of seismic recordings using regression analysis. In order to address the functional form of the models, two common types of magnitude scaling are used in attenuation relations (Bolt and Abrahamson, 2003). The simplest form describes the shape of the attenuation with distance to be independent of the magnitude, such that, the at any distance from the seismic source, the curves maintain a constant shape (Bolt and Abrahamson, 2003). Alternatively, the more complex form describes the shape of the attenuation with distance to be dependent on the magnitude, such that, at close distances to the seismic source, the curves pinch closer together (Bolt and Abrahamson, 2003).

This is due to the saturation of ground motion, indicating that moderate magnitude earthquakes produce similar levels of shaking intensity as larger magnitude earthquakes (Bolt and Abrahamson, 2003). There are also attenuation relations that use a combination of these two models where moderate magnitude earthquakes (for example, $M < 6.5$) have constant attenuation shapes and large magnitude earthquakes (for example, $M > 6.5$) take into account ground motion saturation near the seismic source (Bolt and Abrahamson, 2003). Campbell (2003) described the most common and simplest form of attenuation relation as:

$$\ln Y = c_1 + c_2 M - c_3 \ln R - c_4 R + c_5 F + c_6 S + \varepsilon,$$

where: Y is the strong motion parameter of interest; M is the magnitude; F is the faulting mechanism of the earthquake; S is a description of the **local site conditions** beneath the site; ε is a random error term with a mean of zero and a standard deviation of $\sigma_{\ln Y}$ (the standard error of estimate of $\ln Y$); r is a measure of the shortest distance from the site to the source of the earthquake; and, c_{1-6} are coefficients that depend on the tectonic environment of the regions where the earthquake occurred. Using statistical fitting procedures, such as minimum least squares or maximum likelihood, regression analysis is used to determine the best estimates for coefficients c_{1-6} (Campbell, 2003). Boore et al. (1997) used the simple attenuation form to develop the BJK97 ground motion relations:

$$\mu(M, r_{jb}, V_s) = b_1 + b_2(M - 6) + b_3(M - 6)^2 + b_4 \ln((r_{jb}^2 + h^2)^{0.5}) + b_5 \ln(V_s/V_a),$$

where: μ is the predicted natural logarithm of the ground motion parameter (peak ground acceleration or PGA); M is moment magnitude; r_{jb} is the closest distance (km) to the vertical projection of the rupture; V_s is **the average velocity of seismic shear waves**

through the upper 30 m of the subsurface (V_s30). Other parameters, such as b_{1-5} , h and b_v , are solved in the regression with empirical data (Boore et al., 1997).

There are several methods used in the theoretical approach for predicting expected ground motion. Some complicated approaches involve kinematic and dynamic methods (Somerville et al., 2001; Campbell, 2003). The most basic approach is referred to as the stochastic model, which predicts the ground motion level as a function of magnitude and distance (Campbell, 2003):

$$A(f) = Src(f)Attn(f,R)Amp(f),$$

where: $Src(f)$ describes the earthquake source (source effect); $Attn(f)$ describes the attenuation caused by wave propagation through the crust (path effect); $Attn(R)$ describes the distance parameter, accounting for geometric attenuation; and $Amp(f)$ describes the response of the materials beneath the site (**site effect**). The Atkinson and Boore (1997) attenuation relation is an example of a stochastic approach to estimating a predicted ground motion.

Early on, because of the complexity in the approach and the need for detailed sub-surface information, Joyner and Fumal (1984), and, Joyner and Boore (1988) were the only practitioners to include effective velocity (see Appendix A) as a site effects parameter in their empirical (statistical) attenuation relations (Wills et al., 2000). Later, this method found use in the calculation of site amplification in the theoretical (stochastic) ground motion approaches (for example, Atkinson and Boore (1995; 1997)).

Amplification of Seismic Waves The effects of site amplification from strong ground motion have been observed from the earthquake damage (Wood, 1908; Reid, 1910) and in the seismic records (Borcherdt, 1970; Boore and Joyner, 1997).

Theoretically, as referred in the stochastic attenuation model, site response, or amplification, is given by (Campbell, 2003):

$$Amp(f) = \sqrt{\frac{\rho\beta}{\rho_s(f)\beta_s(f)} \exp(-\pi\kappa_0 f)},$$

where: β is the density of the crust beneath the site; ρ is the shear wave velocity; $\rho_s(f)$ is the effective density; $\beta_s(f)$ is the effective velocity; and κ is the site damping factor obtained from recordings (Anderson and Hough, 1984; Hough et al., 1988) or inferred from empirical ground motion models (Boore et al., 1992; Schneider et al., 1993).

Alternatively, amplification factors can be derived from regressions of large volumes of data. For example, using data recorded from the TriNet project (Heaton et al., 1996), Tinsley et al. (2004) solved for unknown amplitudes and optimum paths and yielded residuals, from the magnitude determinations, that presumably reflected the full range of site effects, including shallow-layer resonances (for example, Hartzell et al. (2003)), basin-edge effects (for example, Frankel et al. (1991)), and near-site attenuation (for example, Anderson and Hough (1984)).

Another approach for characterizing site amplification is to correlate the effects of surface geology (local site conditions) on ground motions (Borcherdt, 1970; Fumal and Tinsley, 1985; Boore and Joyner, 1997; Wills et al., 2000; Wills and Clahan, 2006). Theoretically, the composition of the geologic material can be expressed simply in terms of the material's mechanical behavior or response to seismic disturbance (Gueguen and Palciauskas, 1994). Specifically, this behavior is expressed as the material's elastic constant (M) and density (ρ) which generally depend on lithology (Gueguen and Palciauskas, 1994). To diagnostically relate the acoustic rock properties (velocity and

attenuation) to the rock type, Hooke's Law must first be considered (Gueguen and Palciauskas, 1994):

$$\varepsilon = \frac{\sigma}{M},$$

where: ε is dimensionless; σ is the stress applied (Pa or bar); and M is the solid's elastic modulus (Pa or bar). Since anelastic damping, or the factor-Q, is primarily affected by the shear component of the strain (Lowrie, 1997) and because there are fundamentally two elementary stress states and two distinct moduli, only shear deformation and its distinct modulus is considered here (Gueguen and Palciauskas, 1994):

$$\mu = \frac{\sigma}{2\varepsilon}, M = 2\mu.$$

Next, by considering shear deformation propagating along the x-axis (arbitrary), the displacement is given as (Gueguen and Palciauskas, 1994):

$$u_y(x,t) = e^{i(kx - \omega t)}$$

Then, consider (Gueguen and Palciauskas, 1994):

$$\varepsilon_{xy} = \frac{1}{2} \frac{\partial^2 u_y}{\partial x^2}$$

and

$$\sigma_{xy} = \mu \frac{\partial u_y}{\partial x},$$

such that:

$$\frac{\partial \sigma_{xy}}{\partial x} = \rho \frac{\partial^2 u_y}{\partial t^2}.$$

The propagation for the shear wave (V_s) becomes:

$$\mu = \frac{\partial^2 u_y}{\partial x^2} = \rho \frac{\partial^2 u_y}{\partial t^2}$$

and the V_s can be given as:

$$V_s = \sqrt{\frac{\mu}{\rho}} .$$

On the basis of this simple relationship, the known shear-wave velocity of rock types (lithology) from laboratory measurements is extended to correlate to two classes of rocks: sedimentary and igneous. For example, Press (1966) observed that seismic velocities are greater in volcanic rocks than in sedimentary deposits, with granitic rocks having higher velocities than andesites and that unconsolidated sediments have lower velocities than sedimentary rocks, while surface alluvium and loose sands have lower compressional velocities than clays (water-saturated clays have the lowest shear velocities of all rocks) (Hatheway and Kiersch, 2000). Fundamentally, there are three general types (sedimentary, igneous and metamorphic) of rock, but in practice, only sedimentary and igneous rocks are considered. This is because: (1) igneous rocks represent 95% of the Earth's crust by volume; and (2) approximately 75% of the continental surfaces and almost all of the ocean floor is covered by sedimentary rocks with thicknesses that averages 2 km over continental surfaces and approximately 1 km on the ocean floor (Pettijohn, 1975; Gueguen and Palciauskas, 1994). Due to the relative paucity of the metamorphic rocks in the crust, it is treated as an evolutionary stage of sedimentary rocks (Gueguen and Palciauskas, 1994). On the basis of the aforementioned relationships and work from numerous studies, the correlation between the effects of the materials from surface geology on V_s is established.

Local site conditions describe the materials that lie directly under the site. Preferably, these descriptions extend to the depth of the basement rock although a depth to no less than 30 m is sufficient (Anderson et al., 1996). These descriptions are usually

defined in terms of: (1) surface or near-surface geology; (2) shear-wave velocity; and (3) the depth of the sediments beneath the site (Campbell, 2003). Shear-wave velocity and sediment depth are preferred (Campbell, 2003) because these parameters can be directly applied to attenuation relations to account for the dynamic response below the site (Boore and Joyner, 1997). To classify a site based on shear-wave velocity, two methods are used (Campbell, 2003): (1) the average velocity of seismic shear waves through the upper 30 m of the subsurface (V_{s30}); or (2) the effective velocity from the surface to a depth corresponding to a quarter wavelength of the period or frequency of interest (Boore and Joyner, 1991). Site categories based on V_{s30} were first used by Boore et al. (1993) in the development of attenuation relations (Campbell, 2003). The V_{s30} method is given by (Campbell, 2003):

$$V_{s30} = \frac{\sum_{i=1}^n d_i}{\sum_{i=1}^n d_i / V_{si}},$$

where: d_i is the thickness; V_{si} is the shear-wave velocity of soil layer i ; and progressively deeper soil layers are incorporated until the summation in the numerator equals 30 m. This method is the preferred parameter for engineering analysis because it is adopted in all U.S. building codes. Alternatively, Joyner et al. (1981) proposed the use of the effective velocity, or quarter-wavelength method, to parameterize shear-wave velocity (V_{si}) and depth (d_i), based on observations that “site amplification may be less a matter of resonance involving reinforced multiple reflections and more the simple effect of the low near-surface velocity”. The depth is given by (Campbell, 2003):

$$D_{1/4}(f) = \sum_{i=1}^n d_i,$$

where: $T = 1/f$ is the period of interest. Progressively deeper soil layers are used in the above summation until the equality (below) is met (Campbell, 2003):

$$\sum_{i=1}^n d_i/V_{Si} = T/4.$$

Early on, because of the complexity in the approach and the need for detailed subsurface information, Joyner and Fumal (1984), and, Joyner and Boore (1988) were the only practitioners to include effective velocity (see Appendix A) as a site effects parameter in their empirical (statistical) attenuation relations (Wills et al., 2000). Later, this method found use in the calculation of site amplification in the theoretical (stochastic) ground motion approaches (for example, Atkinson and Boore (1995; 1997)).

In addition, there are other site conditions, such as topographic (for example, Kawase and Aki (1990)), basin-edge (for example, Bard and Bouchon (1980)), resonance (for example, Anderson and Hough (1984)) and other factors, that will notably affect the response of the ground during seismic excitations, but these conditions are not discussed in this project.

APPENDIX B

Remote Sensing Principles

Remote sensing is defined as the unobtrusive detection of information about the existence of an object without being in direct physical contact with the object of interest (after Elachi and van Zyl (2006)). The detected information is about the changes that the object imposes on its surrounding environment; where, geophysical phenomena, such as electromagnetic (EM), acoustic or potential fields exist (after Elachi and van Zyl (2006)). Remote sensing platforms on-board space-borne or air-borne crafts are commonly used to operate detection and recording systems that monitor planets and their environment. Examples about the remote sensing of EM, acoustic and potential fields include (respectively): the detection of synthetic aperture radar (SAR) based on interferometry (If), seismic reflection/refraction investigations and the subsurface imaging of electrical resistivity (ER). All three methods vary in degrees of obtrusion, as in other types of remote measurements, and all three methods use inversion techniques to analyze and interpret the original data. An important distinction about IfSAR, and other similar systems, is that its field of measurement is created from an active source, where radar pulses, usually generated from the remote sensing platform aboard an aircraft or satellite, is actively emitting pulses, to interact with the object; then each pulse is reflected back and recorded by the platform's signal collector for measurement. Similarly, some seismic reflection/refraction investigations employ active sources, such as man-made explosions, to record seismic velocities. On the other hand, ER measurements are commonly acquired by the detection of perturbations in the electric potential field (passive source) at the near-surface (Lowrie, 1997). In this project, remote sensing is

defined as a satellite-based imaging spectrometer system that detects reflected and emitted electromagnetic radiation (EMR), in the visible (VIS) to the thermal infrared (TIR) wavelengths (0.4-14 μm), through illumination from solar radiation (passive source) (Liang, 2004).

The Remote Sensing System Fundamentally, a remote sensing system consists of (1) a source of radiant energy, (2a) an object that interacts with the radiated energy or (2b) an object that is itself a source of radiant energy, (3) a resultant radiance from the object, and (4) a sensor that detects the radiance captured by a collector and (5) measures the properties of the radiance (Elachi and van Zyl, 2006).

The Spectral Source and Spectra In a remote sensing system, solar radiation is the most common source of radiant energy that incites an object to impose change to its surrounding field. This energy is EM by nature and is fed by the entire spectrum of EM radiation generated from the thermonuclear reactions taking place on the surface of the Sun (Jensen, 2000). Although the EM radiation consists of a continuous spectrum that ranges from short bandwidths of very high frequency ($\sim 10^{20}$ Hz) in the gamma ray region, to long bandwidths of very low frequency ($\sim 10^3$ Hz) in the long radio wave region (Jensen, 2000), this project only considers spectra that are located in the visible to thermal infrared ($\sim 10^{18}$ - 10^{23} Hz) bands.

The visible to thermal infrared regions are commonly divided into ranges of wavelengths based their characteristic properties. The visible (VIS) region is the portion (0.4-0.7 μm) of the EM spectrum where the human eye perceives colors from viewing objects (Aronoff, 2005). These characteristic properties are illuminated by reflected solar energy ranging from purple (0.4-0.45 μm) and blue (0.45-0.52 μm) through green (0.52-

0.6 μm), orange (0.6-0.63 μm) and red (0.63-0.7 μm)(Aronoff, 2005). Just outside of human perception, the infrared (IR) region is the portion (0.7-14 μm) of the EM spectrum where reflected and emitted energy are detected. The reflected solar energy is particularly dominant in the near infrared (NIR) and short-wave infrared (SWIR) regions that correspond to wavelengths of 0.7-1.0 μm and 1.0-3.0 μm , respectively. Where as, the emitted energy, in the mid-infrared (MIR) and long-wave infrared portions, are collectively referred to as the thermal infrared (TIR) region (3-14 μm) and have wavelengths of 3.0-8.0 μm and 8-14 μm , respectively (Adams and Gillespie, 2006). Because the Sun has a dominant wavelength (0.48 μm) in the VIS range (0.4-0.7 μm), the VIS and the NIR spectra are the most commonly used bandwidths in modern sensor specifications (Jensen, 2000; Elachi and van Zyl, 2006). Also, since all objects that are able to maintain its temperature above absolute zero (-273°C or 0 K) continuously emit EM energy (Jensen, 2000), additional capabilities to detect spectra in the TIR range are also specified in sensor designs.

Transmission The full spectrum of EMR transmits, practically unperturbed, through the virtual vacuum of space at a velocity of 3×10^8 m/s (speed of light) in the form of energy waves powered by emissions radiated from the Sun. The EMR behaves in accordance with the basic wave theory, which is described as:

$$c = \lambda f ,$$

where: c is the speed of light (3×10^8 m/s); λ is the wavelength (in μm or nm units) ; and f is the frequency (Hz). In remote sensing applications, the EM wave is commonly referred to by its location on the EM spectrum, in terms of its bandwidth or range and also by its wavelength or frequency. After entering the Earth's atmosphere, the radiant

energy encounters objects that cause the energy to be absorbed, refracted, scattered or reflected.

Absorption Absorption is the process by which EM energy is absorbed and subsequently, converted to another form of energy, such as heat (Jensen, 2000). The object, be it atmospheric particles or terrain elements, has a unique set of wavelengths or frequencies where EM energy is preferentially absorbed (Jensen, 2000). Absorption occurs when the incident energy with the same frequency as the resonant frequency of the object comes into contact. The absorption produces an excited state in the atom or molecule and instead of reradiating the photon with the same wavelength, the energy is transformed into heat energy and reradiated at a longer wavelength (Jensen, 2000). These regions of absorption are referred to as absorption bands and are critical for identifying an object of interest. For example, minerals have unique absorption characteristics in specific portions of the EM spectrum that allow their identification (Jensen, 2000). On the other hand, the cumulative effect of the aerosols in the atmosphere and other constituents can cause portions of the spectrum to transmit ineffectively. Noteworthy is the VIS (0.4-0.7 μm) region of the spectrum where wavelengths are very effectively transmitted by the Earth's atmosphere and is referred to as an atmospheric window.

Reflectance Reflectance is the interaction between matter and the waves of the EMR, whereby after the interception of the radiating energy by the matter, the energy is "bounced off" the surface of the matter (Jensen, 2000). As a fundamental characteristic of reflectance, the incident radiation, the reflected radiation, and the vertical from the

surface all lie in the same plane. In addition, the angle of incidence and the angle of exitance (reflectance) are equal when measured from the vertical (Jensen, 2000).

Various types of reflections depend on the reflecting surfaces. Specular reflection occurs from a smooth surface when the average surface profile height is several times smaller than the wavelength of the radiation intercepted by the surface; such that, the reflection yields a mirror image (Jensen, 2000). Calm water bodies are conducive to near-perfect, specular reflection of incidental radiance (Jensen, 2000). Diffuse reflection occurs from a rough surface when the average surface profile height is several times larger than the wavelength of the radiation intercepted by the surface; such that, the reflection does not yield a mirror image (Jensen, 2000).

Scatter Scatter differs from reflection in that the direction associated with scattering is unpredictable (Jensen, 2000). Various types of scatter, primarily occurring in the atmosphere, depend on the kind of aerosols encountered in the atmospheric column. To a lesser extent, the lack of individual reflecting surfaces or non-aerosols may also cause the scattering of exitance radiance outside of the atmospheric column (Jensen, 2000).

Raleigh scattering, or molecular scattering, occurs at the upper 4 km of the atmospheric column, where the effective diameter of the matter, e.g., gas molecules, is many times smaller than the wavelength of the radiation (Jensen, 2000).

Mie scattering, or non-molecular scattering, occurs at the lower 4.5 km of the atmospheric column, where the effective diameter of the matter, e.g., smoke and dust particles, is equal to the wavelength of the radiation (Jensen, 2000).

Non-selective scattering occurs at the lowest part of the atmospheric column when the effective diameter of the matter, e.g., water molecules, is many times larger

than the wavelength of the radiation intercepted by the surface of the matter, such as water droplets and ice-crystals (Jensen, 2000).

APPENDIX C

ASTER Remote Sensing System

The remote sensing data in this project are based on electromagnetic spectra recorded by the ASTER (Advanced Space-borne Thermal Emissions and Reflectance) radiometric instruments on-board the Earth Observing System (EOS) AM-1 platform of the Terra satellite. Terra's flight path is sun-synchronous and has a circular, near-polar orbit at an altitude of 750 km. Its equatorial crossings are at the local time of 10:30 a.m. and returns to the same orbit at every 16th day. The AM-1 platform includes other remote sensing systems, such as the Moderate-Resolution Imaging Spectrometer (MODIS), the Multi-angle Imaging Spectro-Radiometer (MISR), the Clouds and the Earth's Radiant Energy System (CERES), and the Measurements of Pollution in the Troposphere (MOPITT) instrument (Abrams et al., 2002). As the only high spatial resolution (15 m) instrument on board, ASTER is the "zoom lens" for these other sensors, viewing the ground in 60 km X 60 km swathes (Abrams et al., 2002). The ASTER instruments were constructed by a consortium of the top Japanese electronics commercial manufacturers that included the Nippon Electric Company (NEC), Mitsubishi Electric Corporation (MELCO), Fujitsu and Hitachi, with Japan's Ministry of Economy Trade and Industry (METI) and the Japan Resources Observation System organization (JAROS) managing the overall project. ASTER was launched in December 1999 onboard the National Aeronautic and Space Administration (NASA) EOS series satellite Terra (Abrams and Hook, 1995). This on-going joint venture represents an international cooperative between the U.S. scientific/space agency and the Japan industrial/governmental group (Yamaguchi et al., 1998; Abrams et al., 2002). Together,

the main mission, comprising of the ASTER Science Team (NASA) and the ASTER Instrument Project (METI), is to improve the understanding of local- and regional- scale processes based on the observations of the land surface, biosphere, solid Earth, atmosphere and oceans (Yamaguchi et al., 1998; Abrams et al., 2002). ASTER data was first released in November 2000 from the ASTER Ground Data System (GDS) of the Earth Remote Sensing Data Analysis Center (ERSDAC) of Japan and from the Earth Resource Observation System (EROS) Data Center (EDC) of the U.S. Geological Survey.

The ASTER detection and recording system is consist of a set of four optical telescopes that collect spectra in three separate recording subsystems (Abrams et al., 2002). The visible and near-infrared (VNIR) system records four discrete bandpasses (channels 1, 2, 3N, and 3B) that are collected from two separate telescopes: a nadir-viewing telescope that records channels 1, 2, and 3B; and, a backward-viewing telescope that records channel 3B (Abrams et al., 2002). Both telescopes can be rotated ($\pm 24^\circ$) as a unit and have spatial resolutions of 15 m (Abrams et al., 2002). The shortwave infrared (SWIR) system records six discrete bandpasses (channels 4-9) that are collected from a fixed viewing telescope that uses an adjustable ($\pm 8.54^\circ$ from nadir) scanning mirror for rotation and has a spatial resolution of 30 m (Abrams et al., 2002). Also using an adjustable scanning mirror with in the same rotational range, the thermal infrared (TIR) channel system records five discrete bands (channels 10-14) and has a spatial resolution of 90 m (Abrams et al., 2002). Although the spectral resolution is sensitive to wavelengths (0.52 to 11.65 μm) from the VNIR to TIR spectral range, each ASTER channel was purposely designed to record the spectrum in a discrete manner (Abrams et

al., 2002). These bandpass windows optimize the recordable information in select regions of the spectrum: (1) where the measurable emitted and reflected radiances and temperature are most distinctive for spectral discrimination of surficial materials; and (2) for stereoscopic correlations to construct digital elevation models (DEM) (Abrams and Hook, 1995).

After the spectra is recorded on board the satellite, the ASTER system sends the original data, in raw digital counts, along with the radiance calibration information, to the Tracking and Data Relay Satellite System (TDRSS) facility at White Sands, New Mexico. It is then ground-shipped to the EOS Data Operations Systems (EDOS) at the Goddard Spaceflight Center (GSFC). Here, EDOS sends two streams of data: an 'expedited stream' of data to the EDC LP-DAAC, for rapid processing if needed; and a 'production stream' of data (by airfreight) to the ASTER GDS in Japan for 'routine' preprocessing. After this, the GDS ships (by airfreight) the processed data products to the U.S. Geological Survey's Land Processes Distributed Active Archive Center (LP-DAAC) for ingestion, archive and distribution. The LP-DAAC is also responsible for processing the GDS data products to higher-level 'on-demand' products.

The ASTER system was not designed to continuously record and send data, so acquisition schedules were generated at GDS with inputs from Japan and the U.S; hence, data was acquired 'on-demand'. In the past, most data acquisition requests (DAR) involved 'on-demand' data for coverage that was not previously recorded. It was only recently, when enough data were acquired that there is now global coverage by ASTER data. Effectively, the use of on-demand in ASTER terminology, in reference to a specific, mission-directed acquisition of missing or future coverage, will eventually be

superceded by its other meaning, describing higher level data products with parameterizations like: brightness temperature, reflectance, radiance, emissivity, decorrelation stretches, etc. Essentially, ASTER produces three levels of data products and are either designated as routine or on-demand (Abrams et al., 2002). Each level of product has characteristics based on different parameterizations, but all data products represent the level of processing applied to the Level-1A (AST_L1A) data, which was reconstructed from the raw digital counts at the Level-0 granule, as recorded by the ASTER subsystems (Abrams et al., 2002). With the exception of the popular geo-encoded 16-bit Tagged-Image File Format (TIFF) used in the ASTER Level-3 DEM product (AST14DEM), all ASTER data products use the Hierarchical Data Format-Earth Observation System (HDF-EOS) standard developed specifically by NASA for the EOS missions (Abrams et al., 2002). The HDF-EOS (.hdf) data product is accompanied by a metadata file (.met), which contains standardized attribute information about the image product. The TIFF (.tif) data product is also accompanied by a standardized metadata file but with a slightly different file extension name (.tif.met) and is similar to the more popular world file format (.twf).

For U.S. data users, the LP-DAAC is the sole point of distribution for the routine and on-demand data products. Cost of data is on a per-image basis from the EOS Data and Information System's (EOSDIS) EOS Data Gateway (EDG) web-portal (<http://edcimswww.cr.usgs.gov/pub/imswelcome/>) (Abrams et al., 2002). For this project, 'routine' mode data products from the EDG, such as ASTER Level-1B (AST_L1B) and ASTER Level-3 (AST14DEM), are used.